Master's Thesis

Experimental Investigations for Heat Transfer Characteristics of Under-expanded Impinging Jet

Dongsu Kim

Department of Mechanical Engineering

Graduate School of UNIST

2017

Experimental Investigations for Heat Transfer Characteristics of Under-expanded Impinging Jet

Dongsu Kim

Department of Mechanical Engineering

Graduate School of UNIST

Experimental Investigations for Heat Transfer Characteristics of Under-expanded Impinging Jet

A thesis/dissertation
submitted to the Graduate School of UNIST
in partial fulfillment of the
requirements for the degree of
Master of Science

Dongsu Kim

01/10/2017 Month/Day/Year of submission

Approved by

Advisor
Jaeseon Lee

Experimental Investigations for Heat Transfer Characteristics of Under-expanded Impinging Jet

Dongsu Kim

This certifies that the thesis/dissertation of Dongsu Kim is approved.

01/10/2017 Month/Day/Year of submission

signature

Advisor: Jaeseon Lee

signature

Hyungson Ki: Thesis Committee Member #1

signature

Jaesung Jang: Thesis Committee Member #2

signature

_____

typed name: Thesis Committee Member #3

signature

_____

typed name: Thesis Committee Member #4;

three signatures total in case of masters

Abstract

In this study, under-expanded impinging gas jets are investigated experimentally for understanding heat transfer characteristics of the jets. As working fluids, nitrogen (N_2) and carbon dioxide (CO_2) are selected in order to observe heat transfer effect changed by different working fluid. CO2 jet has a potential way to enhance the heat transfer effect which is sublimation. The novel concept of dry-ice assisted jet impingement cooling is proposed in this study. When carbon-dioxide (CO_2) passes through a tiny orifice gap or jet nozzle, it experiences a rapid temperature drop as well as a pressure decrease via the Joule-Thomson effect. Joule-Thomson coefficient of CO_2 is proven to be higher than the coefficient of other gases' such as nitrogen, hydrogen, air. This temperature drop causes the formation of small CO_2 dry-ice particles. In addition to the enhanced cooling performance caused by lowered bulk-jet temperature, heat transfer is improved by the additional sublimation effect between the dry-ice particles and the cooling target surface. A comparison of the cooling performance between the suggested CO_2 solid-gas two-phase jet and a single-phase nitrogen (N_2) jet was performed experimentally as well.

In order to form dry-ice particles, high pressure and velocity of jet fluid are inevitably required, which is enough for compressible effect to appear. Both jets have differences not only in phase change but also in jet flow structures. As jet velocity increased, shock structures at jet downstream appeared and surface temperature is changed as well. The structures are detected more clearly in N_2 jet than CO_2 jet because of the difference in total pressure at jet boundary, therefore, relationship between shock structure of N_2 jet flow and heat transfer is investigated in this study. In case of high Reynolds number impinging jet which is enough to reach supersonic flow regime, stagnation temperature of impinged surface is affected by jet structure as well as other factors such as nozzle-plate distance or radial distance does. When the jet flow velocity becomes supersonic, shock structures are constructed at downstream of the nozzle exit. Complicated shock structure such as Mach shock disk, plate shock is highly expected to affect to the heat transfer behavior of impingement surface. In this study, a cooling performance of supersonic N_2 jet is investigated by measuring the impinged surface temperature and the flow of the jet is visualized by Schlieren image system. Visualized image and surface temperature are compared to clarify the flow structure-related heat transfer characteristics. In all the experiments of present study, jet fluids are expanded through a circular nozzle and impinged on an electrically heated flat heater surface, and their heat transfer coefficients are measured. The performances of the impinging jet for both fluids are also evaluated via the variance of flow parameters, for example, the Reynolds number, and the jet geometry configurations.

Contents

List of Figures

List of Tables

Nomenclature

Symbol	*Description*	*Unit*
d	Nozzle diameter	[mm]
D	Distance to the mirror	[mm]
f	Focal length of the mirror	[mm]
h	Convective heat transfer coefficient	[W/m^2-K]
i	Enthalpy	[kJ/kg]
i_1, i_2, i_3	Enthalpy of fluid at the chosen point	[kJ/kg]
L	Distance between the nozzle and the test section	[mm]
l_1, l_2, l_3	Distances between thermocouples	[mm]
$\dot{m}$	Mass flow rate	[kg/s]
NPR	Nozzle pressure ratio	[-]
P	Pressure	[kPa]
p_1, p_2, p_3	Pressure at the chosen point	[kPa]
q''	Heat flux through the heater base area	[W/m^2]
Q	Heat applied by ceramic heater	[W]
Re_d	Reynolds number based on the nozzle diameter	[-]
T	Temperature	[K, ℃]
V	Velocity	[m/s]

V_2, V_3	Velocity for flow at the chosen point	[*m/s*]

Greek

μ_{JT}	Joule-Thomson coefficient	[*K/kPa*]
μ	Dynamic viscosity	[*kg/m-s*]

Subscripts

amb	Ambient
aw	Adiabatic wall
i	Beam splitter
in	Nozzle inlet
n	Nozzle
o	Knife edge
out	Nozzle exit
s	Surface

1. Introduction

Impinging jets offer effective transportation of thermal energy or mass via liquid or gas media that is directly blown from orifice(s) or nozzle(s) over the target surface with high momentum flow. Once the fluid media is impinged to a stagnation region on the target surface, both heat and mass transfer occur between the jet bulk-fluid and target surface. The amount of heat transfer at a spot is much high enough to be applicable in industrial processes, such as cooling and/or heating processes. The cooling of a turbine blade, electrical equipment, and critical machinery structures or the heat treatment of material forming processes are potential application fields of impinging jets in industry and widely used. Because the impinging stagnation region is narrow compared with entire surface, an impinging jet is used for thermal management as spot cooling and heating. Effect of the impinging jet on the target surface temperature is one main issue in many application fields because thermal shock or thermal defect conditions of solid surface has an importance to study thermal designs of the surface, thus, prediction of thermal effect of impinging jet is needed.

The characteristics of jet impingement, including heat and mass transfer, were broadly investigated and studied previously [1-4]. Applications and correlations regarding many types of impinging jets were constructed and documented in these past studies. Basic characteristics of impinging jet with circular nozzle configuration are investigated by K. Jambunathan et al [1]. They evaluated heat transfer performance repeatedly but via variation of nozzle geometry and nozzle-to-plate spacing. Based on the study of K. Jambunathan et al, many researchers have designed various experimental settings to figure out heat transfer effect of nozzle geometry (including diameter, length, shape, aspect ratio) [1-2] and several researchers performed experimental studies on impinging jets that include variations of the flow control parameters such as the Reynolds number, jet working fluid properties, etc [3]. The results are presented by relationships between distance and surface temperature (or Nusselt number). Both radial (traverse) distance and height affect heat transfer performance and have a trend which is commonly observed in jet impingement if the values of distances are non-dimensionalized by nozzle diameter [5]. Considering needs of the application fields, some researchers investigated array jets, which are aligned in two-dimension to cool/heat entire surface area. Array jets has parameters which single jet doesn’t have such as jet instance and following cooling performance [6]. The dimensions of the cooling targets have become smaller as micro/nano scale fabrication techniques have progressed, making the impinging jet’s nozzle diameter smaller. As the nozzle diameter and nozzle area decreases, the jet fluid velocity increases, if the flow rate is fixed. This environment creates the need for high-speed impinging micro jets in order to achieve desired amount of heat transfer. Previous researchers have investigated micro-scaled impinging jet, for example, D. Singh [7] performed experiments with different nozzle exit

configurations and Christopher K.W. Tam [5] used different micro-scale nozzle diameter size. Nozzle diameters of micro-jets are incredibly small than usual impinging jets in applications, however, they does not violate an assumption of continuum, so that the result could be comparable to macro-jets previously documented.

These jets can be classified in several ways. One of classification is carried by which phase the jet fluid has. Liquid and gas jets are classified as single-phase jets, if phase changes do not occur during the impinging process, and the jets are classified as two-phase jets if phase changes occur during the impinging process. Single-phase jets are divided into two kind of jets, which are liquid jet and gas jet. Performance of liquid jets is superior to performance of gas jets; however, it has limitations. Working fluid of liquid phase is obligated to be circulated in a closed-loop system. At last, liquid jets need to set up complicated closed-loop system, which requires lots of cares and costs. In addition, jet system confined by wall has corresponding heat transfer effect as well, which are studied by J. San [8]. Also, they are not applicable if the target surface is not allowed to be wet. Many electric components would be in trouble if liquid working fluid is used during cooling process. On the other hand, the gas jets can be used even in open-loop systems which have less labor costs and material, manufacturing processes though they affect much less to heat transfer between the jet fluid and the target surface. Researchers have investigated the characteristics of air jet [9-10] with previously stated experimental parameters.

Different from single-phase jets, two-phase jets utilize the additional latent heat of the fluid between the fluid and the target surface to achieve a higher amount of heat transfer. Several forms of two-phase jets have also been previously investigated [11-15]. Most two-phase jets involve a liquid that experiences evaporation and boiling, including film, transient, or nucleate boiling. Target surface is superheated and low-temperature bulk fluid injected to the surface directly, resulting nucleate boiling phenomena. These jets also need closed-loop system because the portion of liquid phase is not negligible. However, there are two-phase jets which use different kind of working fluids simultaneously. The concept of air jet with water droplet is suggested by Richard [15], which is a spray jet. If possible, gas jet with solid particle that is altered to gas phase due to sublimation could exist.

In that sense, carbon dioxide jet has already shown the possibility of an existence in sublimation-caused two-phase jet. In the case of a carbon dioxide (CO_2) aerosol jet, a surface cleaning technique has been introduced via mass transfer, where contaminants on the target solid surface are removed by the high momentum dry-ice particles that are formed before they impinge upon the surface [16, 17]. The phase change is achieved by characteristics of CO_2's properties. CO_2 is in the gas phase under normal atmospheric conditions, as is the case of many other gases. However, dry-

ice particles can be formed at low temperature below the triple point, *-78.5 ℃*. When CO_2 gas passes through a tiny nozzle or slot, its pressure is drastically decreased after injection. The sudden pressure drop causes a temperature drop as well, such that dry-ice particles could be produced under atmospheric conditions. Regarding heat transfer, the author in this study suggests that once the dry-ice particles and gas-phase CO_2 impinges the target surface at the same time, sublimation of dry-ice simultaneously occurs at the surface, thereby absorbing the additional thermal energy from the target surface. Because the sublimation process is included, heat transfer between the fluid and target surface is expected to be enhanced compared with the case of single-phase jet impingement. Figure 1.1 represents the conceptual schematic of CO_2 solid-gas jet impinging flow. The phase change between the solid phase and gas phase has been rarely discussed in previous studies because the sublimation process is not included in common cases. In particular, developing an understanding of the heat transfer characteristics of two-phase CO_2 jet impingement would benefit from further investigation. In the present study, CO_2 is used as a coolant in an impinging jet to compare its cooling performance with that of another gas, N_2. Both jets are ejected through a circular converging nozzle to experience the desired pressure drop.

The jet flow structure itself is of interest to aerodynamic researchers [18-20]. They performed experimental and numerical investigations on free-jet and impinging jet, focusing on the flow structures and clarifying details of the jet flow structures. Because the nozzle inlet condition is at high temperature and high pressure in some applications, the jet flow might exceed the speed of sound. When this occurs, the compressibility effects arise due to the high momentum of the jet fluid, and complicated shock structures are formed at the downstream of the nozzle exit. Previous investigations on supersonic impinging jets have mainly focused on target surface pressure distribution and flow velocity. As the flow parameters vary, so does the pressure ratio between the nozzle outlet and the ambient environment (NPR), and different types of flow structures are experimentally captured or numerically presented by many researchers [21-24]. Supersonic jets have some trend according to the experimental conditions, pointed out by Y. Nakai et al. [25] who classified the flow structures of under-expanded supersonic impinging jet. Flow field patterns can be predicted if the plate alignment angles, nozzle-plate distance and pressure ratio are provided. They classified three types of shock wave structure of an impinging jet using Schlieren imaging. Also, Angioletti [26] performed numerical simulations and resulted jet flow field patterns.

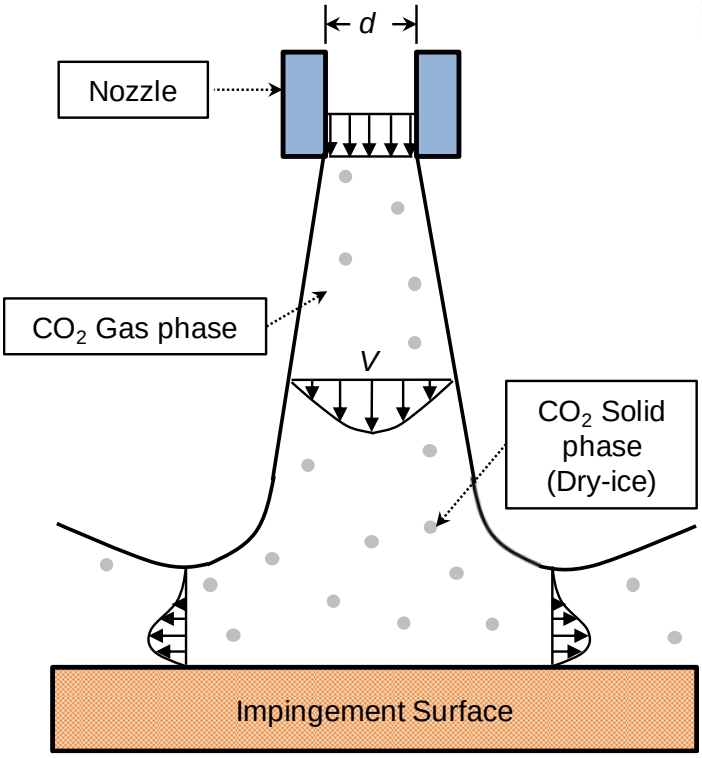

Figure 1.1. Illustration of CO_2 solid-vapor impinging jet

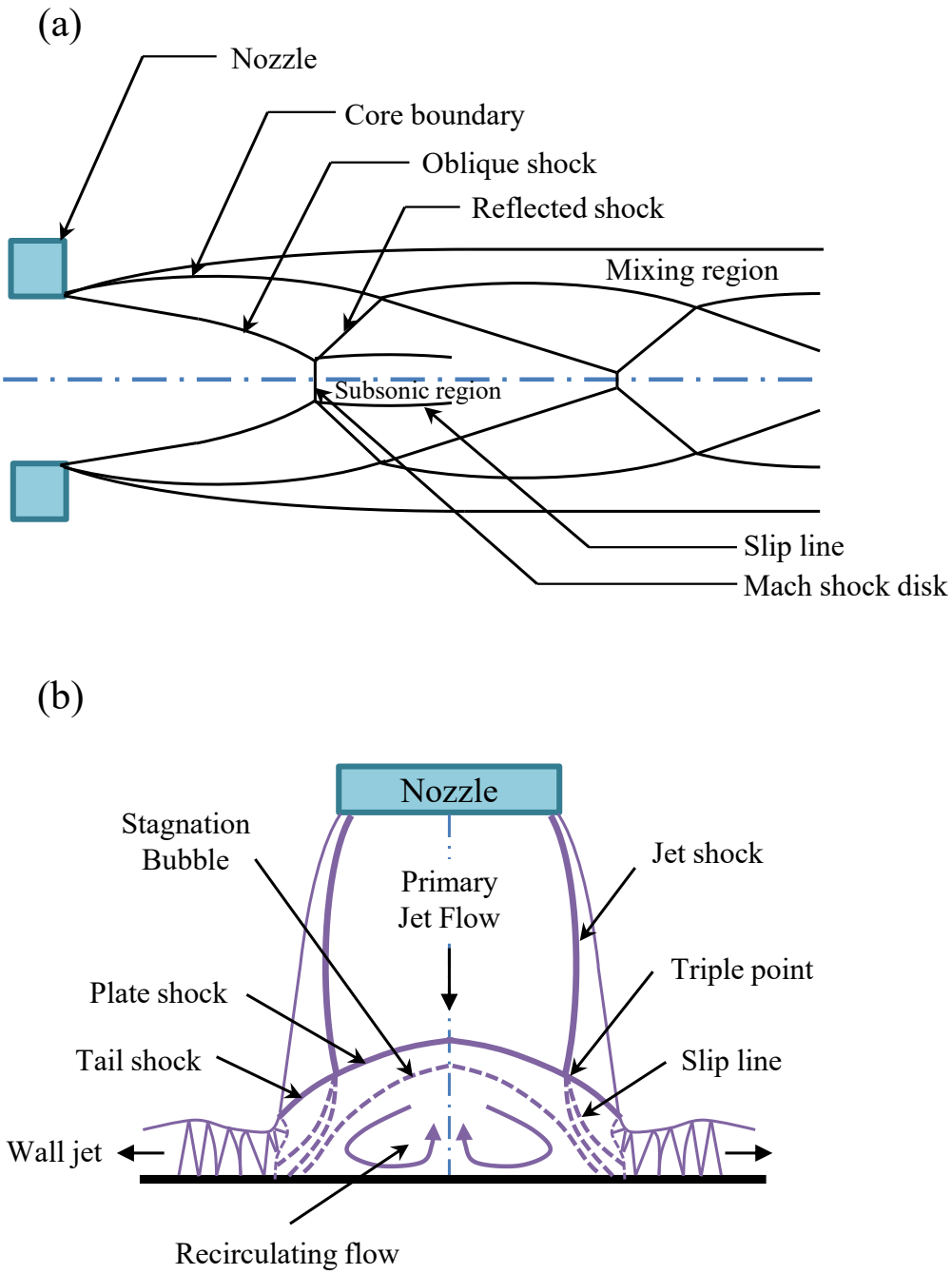

Figure 1.2. Flow structures of supersonic under-expanded (a) free-jet and (b) impinging jet

To obtain an exact understanding of the jet flow structure, including the free-stream and impinging regions, flow visualization techniques are required. There are two main visualization methods, PIV and schlieren shadowgraph. Using these flow visualization techniques, previous researchers visualized the jet flows and observed shock structures of under-expanded supersonic jets. A schlieren imaging is a preferred choice if the interest of the study is the compressibility effect, because it captures shock structures and flow boundaries well by the refraction of the light caused by the knife edge.

The structures are captured and displayed in schematic form. Figure 1.2(a) shows free-jet schematics suggested by T.C. Adamson et al. [19]. At the downstream of the nozzle exit, the jet-ambient air interface has a mixing region, and then core boundaries have a convex structure are shown. Along the jet core center, a supersonic jet flows propagates and meets the oblique shock induced by the nozzle geometry, forming Mach shock disks. The oblique shock results in the continuous reflection of the shock, and the Mach disk makes the stagnation jet flow subsonic. The subsonic-supersonic interface forms a slip line. F.S. Alvi et al. [21] further studied this flow, concentrating on the impingement zone. As Figure 1.2(b) shows, in the impingement zone, surface-related shock structures such as plate shock and tail shock can be observed. As the jet fluid approaches the impingement surface, it experiences plate shock and a drastic deceleration of its speed. Thus, in the impingement zone (stagnation zone), recirculating flows appears instead of high-speed spreading. Supersonic jets have an effect to the target surface in terms of pressure applied. Pressure field around a stagnation point which gets direct jet fluid's momentum have been investigated when the angle of plate varies. Effect of plate angle and impinging jet were discussed by aerodynamic researchers such as M. Dharavath and D. Chakraborty [23], A. Abdel-Fattah et al. [9], J. Song et al. [24].

Though the characteristics of supersonic jets have been previously documented, there is room for further study from the heat transfer point of view. The heat transfer characteristics of a supersonic impinging jet have been investigated by focusing only on the thermal energy transport between the jet fluid and the target surface, and the flow structure investigation has focused only on the pressure distribution on the target surface and the jet flow velocity. The heat transfer between the jet bulk fluid and the impinged surface is not independent of the flow structure but rather expected to be closely dependent. The shock structures constructed at the downstream of the nozzle outlet affect the cooling performance of the target surface. The basic flow structure in this study is shown in Figure 1.3. The heat transfer characteristics of a supersonic circular impinging jet on a flat surface were investigated with a schlieren shadowgraph flow visualization system to determine the relationship between the stagnation surface thermal characteristics and the supersonic shock structure by flow visualization around the stagnation point. The purpose of the present experimental investigation is to suggest a basic concept of the relationship between the supersonic flow structure and the heat transfer

by using stagnation temperature measurements with a flat target surface using a working fluid of nitrogen (N2). In present study, the nozzle exit pressure is enough to achieve high Reynolds number, and the nozzle exit temperature is about ambient temperature at which a gas source is maintained. With these conditions, the cooling performance of the impinging jet is investigated with heated target copper surface.

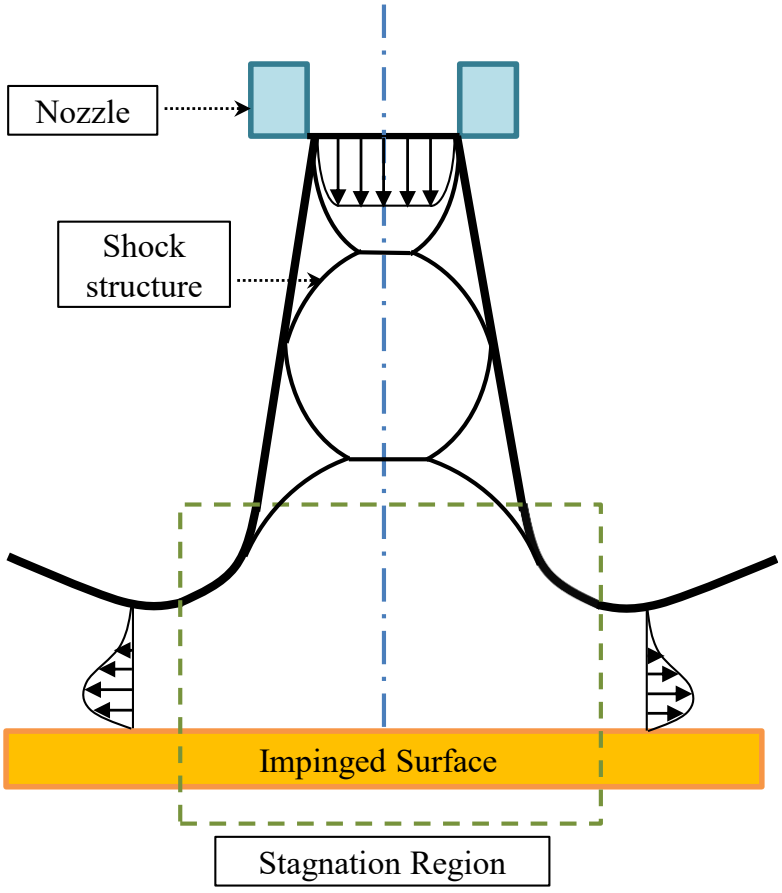

Figure 1.3. Configuration of jet flow for supersonic impinging jet

2. Theoretical Backgrounds

As previously stated, the Joule-Thomson effect has a key rule to form dry-ice particle in CO_2 jet. Regarding this, the magnitude of the Joule-Thomson coefficient is another issue regarding the behavior of CO_2. The temperature change that occurs when a fluid is ejected and expanded through a nozzle is explained by the Joule-Thomson effect. The expansion through a nozzle is considered to be an adiabatic (no heat exchanged) expansion of the gas. In this case, both the pressure and the temperature of the fluid decrease simultaneously.

$$\mu_{JT} = \left(\frac{\partial T}{\partial P}\right)_i \tag{1}$$

In equation. (1), the Joule-Thomson coefficient is defined as the ratio of the temperature variation to the pressure variation. The Joule-Thomson coefficients of some gases are shown in Figure 2.1 [27]. As shown in this plot, the Joule-Thomson coefficient of CO_2 has an especially higher magnitude compared to those of the other gases. As a result, the temperature drop of CO_2 is larger than those of the other gases if the pressure declines by the same amount. Ruebuck *et al.* [228] and Burnett [29] evaluated the Joule-Thomson coefficients of CO_2 with a pressure of 1 *atm* and higher, including the case in which CO_2 liquefies. As the pressure of CO_2 increases, the Joule-Thomson coefficient drastically decreases and then remains almost constant until CO_2 reaches its triple point. In our study, the pressure of the CO_2 is not significantly high after expansion, even though the gas source is at high pressure. Liquid CO_2 could exist in this experiment; however, the amount is small enough not to affect the trend.

Accounting for the Joule-Thomson effect, Sherman [16] discussed the dry-ice forming process when CO_2 is expanded through a nozzle in terms of the thermodynamic properties of CO_2. Sherman [16] explained the phase change of CO_2 according to the state of the gas source. In present experiment, the CO_2 source is a gas-fed source whose quality is *1.0* because only the gaseous part of the CO_2 cylinders is connected to the tubes. Two expansions occur while the fluid flows from the cylinder to the nozzle in the present study. One of the expansions occurs in the regulator connected to the cylinder; this expansion involves a throttling process. The initial state of the gas-fed source is point 1 in Figure 2.2. However, the pressure is decreased while the enthalpy is held constant until the state of the fluid after the regulator reaches point 2, because the isenthalpic characteristic of the throttling process is ideal. The amount of pressure reduction varies widely depending on the volume flow rate and Reynolds number from the regulator. Afterwards, the pressure is decreased again via flow through the converging nozzle until the CO_2 reaches atmospheric pressure.

During flow through the nozzle, in this case, the process is not a constant enthalpy process

because the velocity change is no longer negligible. For the second expansion, the 1st law of Thermodynamics is reduced as

$$0 = \dot{m}(i_2 + \frac{V_2^2}{2} - i_3 - \frac{V_3^2}{2}) \quad (2)$$

In addition, the pressure drop to atmospheric pressure causes an increase of the velocity of the carbon dioxide according to Bernoulli's Equation along the streamline if the difference of gravitational term and frictions are neglected:

$$p_2 + \frac{V_2^2}{2} = p_3 + \frac{V_3^2}{2} \quad (3)$$

The equation shows that the velocity of the nozzle exit is much larger than the velocity of the nozzle inlet, resulting in an enthalpy decrease as CO_2 gas passes through the nozzle. As a result, the final state of CO_2, point 3, is inside the solid-vapor dome, thereby explaining the dry-ice formation. During process 2-3, liquid CO_2 is converted into a solid at the interface between the liquid-vapor dome and solid-vapor dome.

To compare the cooling performance with and without dry-ice assistance, a nitrogen jet is selected in the experiment. Unlike CO_2, N_2 does not experience a phase change due to the state of its triple point, *63.151 K* and *12.52 kPa*. Furthermore, the Joule-Thomson effect of N_2 is expected to be lesser than that of CO_2. Table 2.1 [27] shows some of the thermodynamic properties of N_2 and CO_2 under atmospheric conditions. The Joule-Thomson coefficient of CO_2 differs from that of N_2, which is over 4 times that of N_2. Although other properties have differences, such as density or thermal conductivity, the experimental results are expected to be primarily affected by the difference of the Joule-Thomson coefficients instead of the other properties.

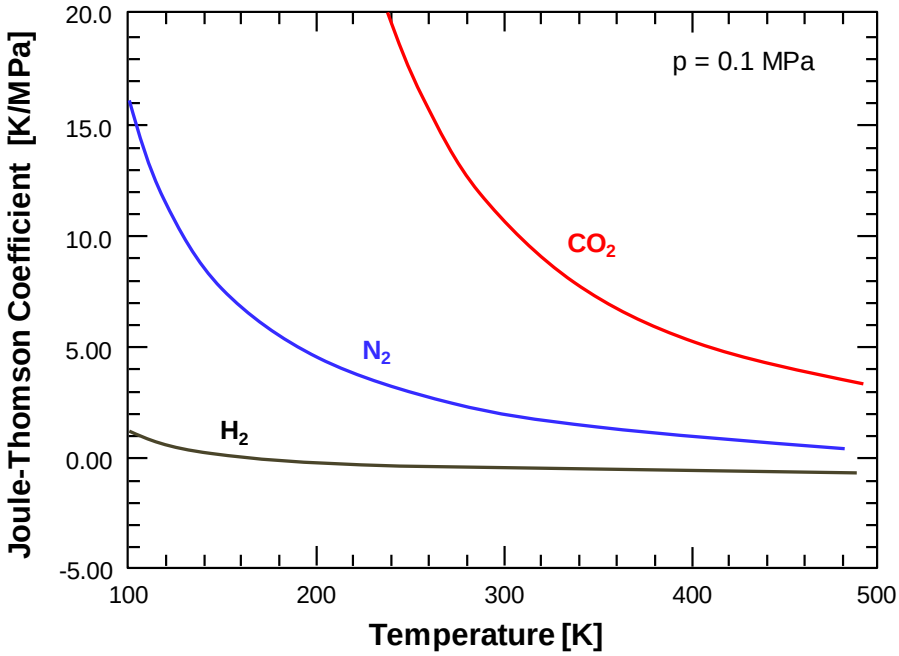

Figure 2.1. Joule-Thomson coefficient of some gases at atmospheric pressure

Table 2.1. Thermodynamic properties of N_2 and CO_2 at *P = 100 kPa* and *T = 23 ℃.*

Gas	Density [kg/m^3]	Viscosity [μPa-s]	Joule-Thomson Coefficient [K/MPa]	Specific Heat [kJ/kg-K]	Thermal Conductivity [mW/m-K]	Prandtl Number
N_2	1.1379	17.712	2.180	1.0413	25.69	0.7179
CO_2	1.7965	14.835	11.122	0.8488	16.48	0.7640

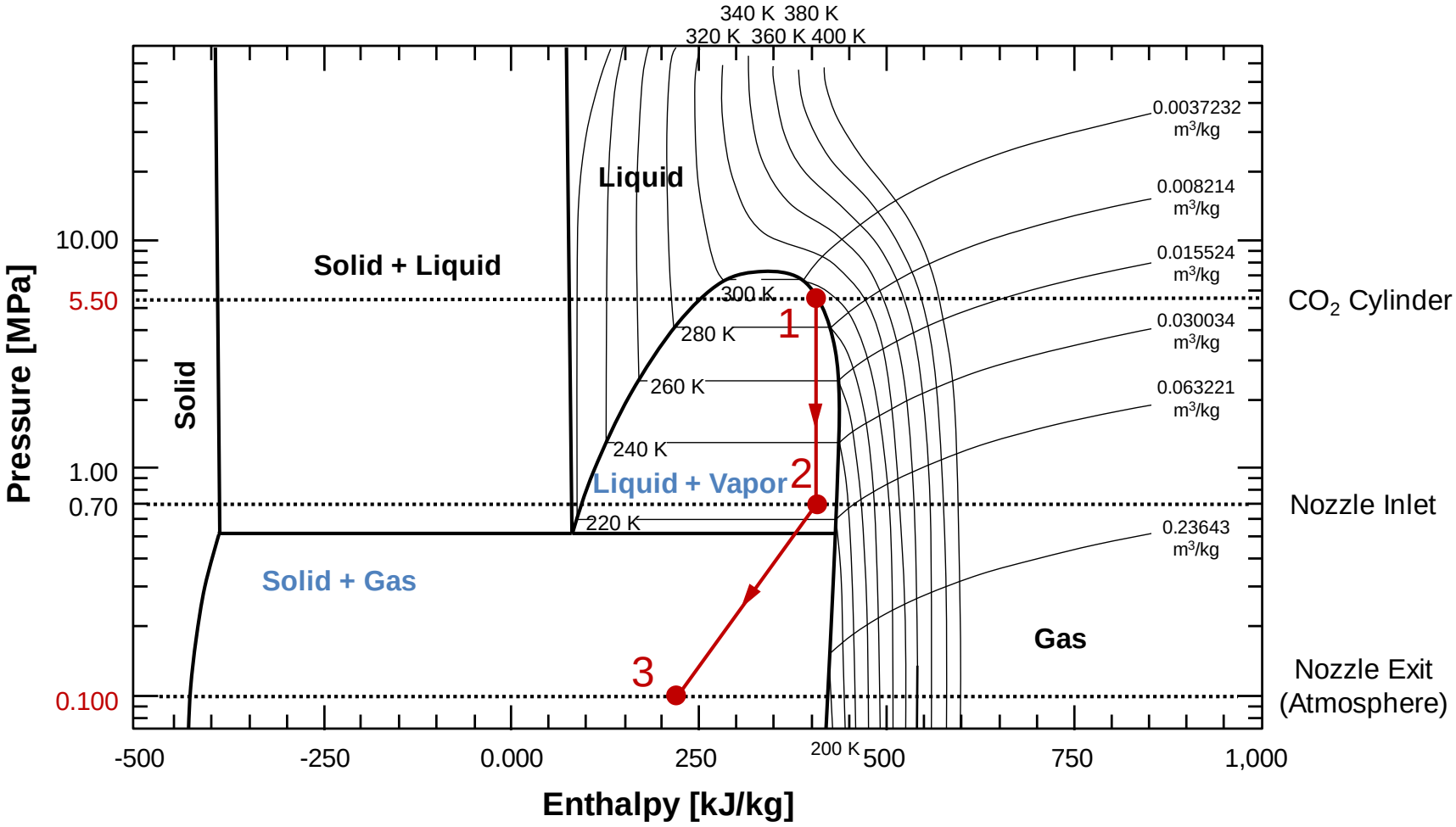

Figure 2.2. Thermodynamic state change of carbon dioxide jet flow in pressure-enthalpy diagram

3. Experimental Setup

Figure 3.1(a) shows a schematic of the experimental apparatus for an impinging jet with two types of testing gases and the data acquisition system. The apparatus is based on a simple open-loop system with single source; N_2 and CO_2 jet are not injected at the same time. The gas source of N_2 and CO_2 are at high-pressure so that the pressure difference between the source and ambient air is high enough to allow the gas to expand through the nozzle. Nitrogen is supplied from large storage vessels and has the pressure of its source maintained at *0.7 MPa*. CO_2 is supplied from 2 small cylinders that contain *20 kg* of high-purity liquid carbon dioxide. Each of the cylinders has a pressure that is originally up to *5.5 MPa*. Both sources are gas-fed, that is, only the gaseous state is supplied to the nozzle instead of the liquid part. Also, there are sensors for measurement of pressure or temperature at nozzle inlet and target surfaces. During experiment, the target surface is captured by IR camera as well. Figure 3.1(b) has minor differences in jet system except for schlieren imaging system. Since schlieren system is positioned both sides of test pieces, great care was taken to set up all the apparatus to capture shadowgraph.

Gas flows in circular tubes with an outer diameter of *6.35 mm*. Tubes and flexible hoses are thermally insulated to minimize the heat transfer from the environment to the gas especially for CO_2 jet experiments. Through the regulator, the pressure of the flow is controlled manually by using a regulator valve. A thermal mass flow meter (Brooks Instrument SLA-5863S) is also installed to monitor and help control the volume flow rate. A pressure transmitter (SETRA-206) and a T-type thermocouple are installed in the tube between the regulator and nozzle to measure the absolute pressure and temperature to determine the conditions at the nozzle inlet. The jet impinges on the test section, which is composed of a copper block with ceramic heater and a surrounding thermoplastic insulator, G10. Four T-type thermocouples were inserted into the heater block to evaluate the surface temperatures and the surface heat transfer coefficient. In addition, an Infra-Red (IR) camera (FLIR-T650SC) is used to measure the temperature distribution around top surface of the test section in 2D, and then, its IR data are transferred to a control laptop computer. The IR images are captured by the camera with tilted angles instead of a right angle. In addition, the emissivity, reference temperature and other settings are calibrated based on the surface temperature measurements from the thermocouples in the copper block. All of the signals from 5 thermocouples, pressure transmitter and flow meter were processed by the data acquisition system through NI-cDAQ 9214 modules.

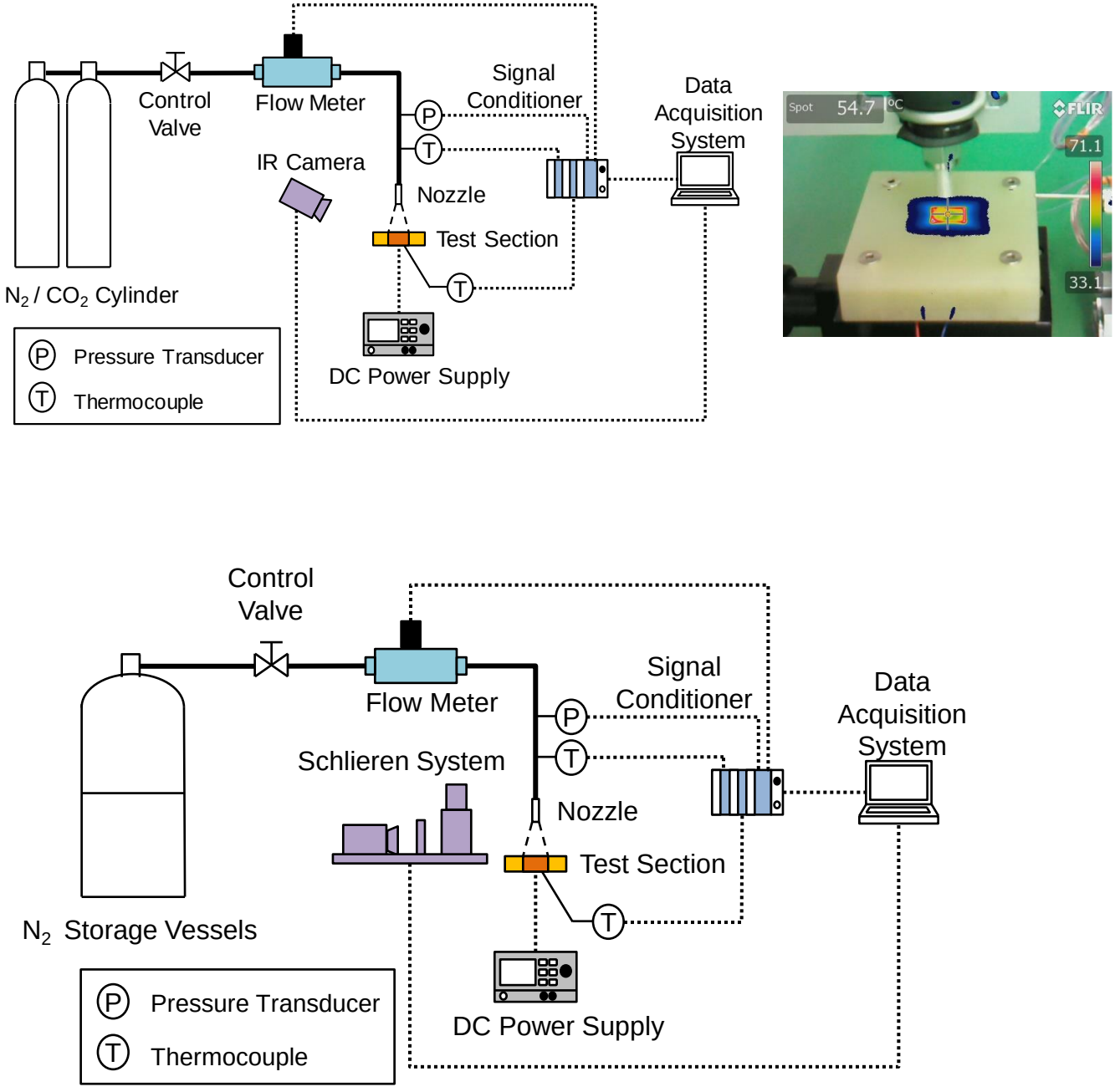

Figure 3.1. Schematics of impinging jet for (a) phase-change experiment with test image (right) and (b) supersonic jet

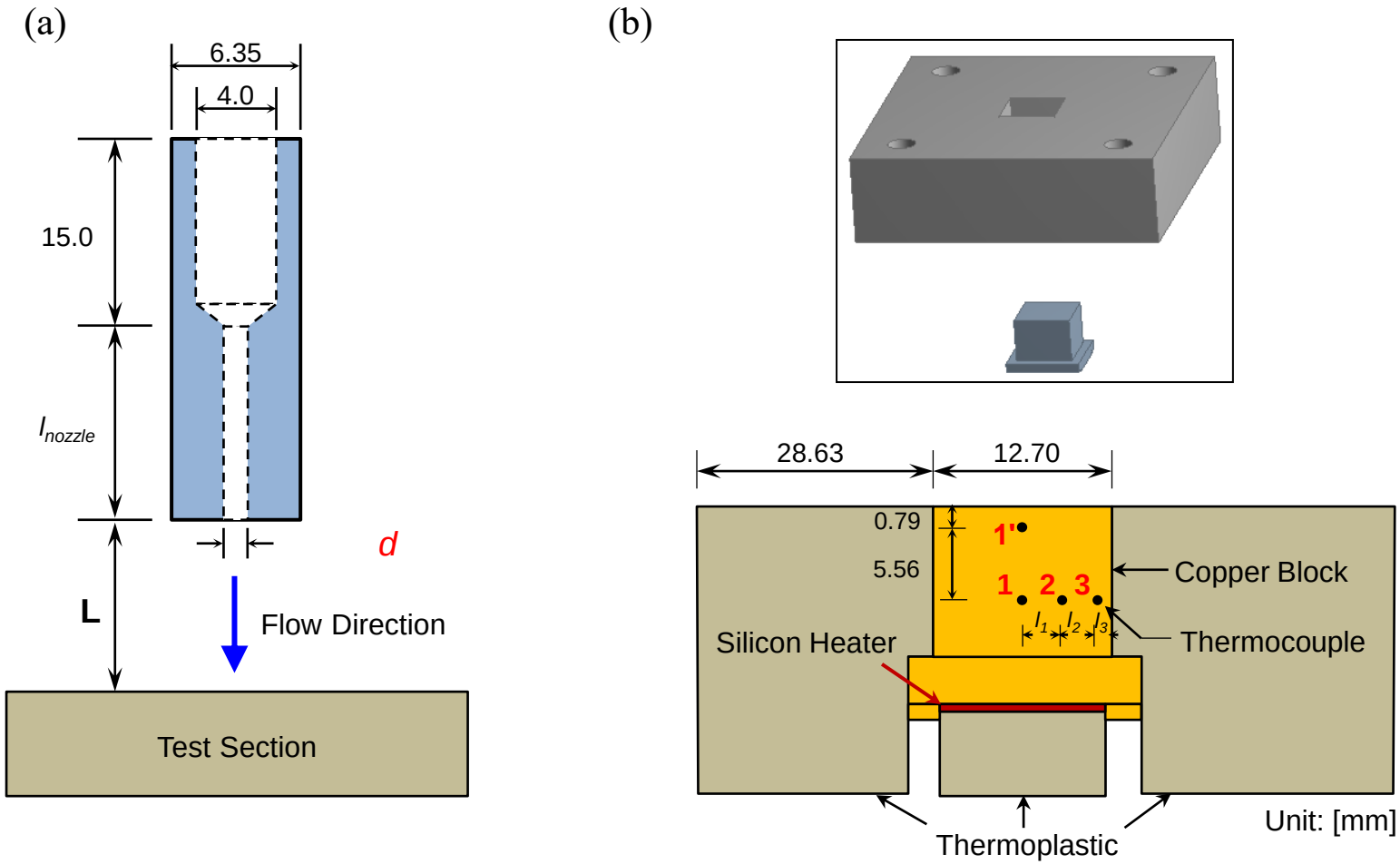

Figure 3.2. Schematics of (a) nozzle geometry, and (b) test section composed of copper block heater and housing with thermocouples inserted

Figure 3.2(a) shows the jet nozzle geometry in detail. The aluminum body nozzle used in this experiment includes two parts that have inner diameters of *4 mm*, for the inlet converging zone and nozzle orifice diameter with a vertical length. The latter inner diameter represents the nozzle diameter, *d*. The values of nozzle diameter and nozzle length varies in each experimental condition and parametric study. The nozzle inlet geometry is a simple converging structure, for which the diameter is decreasing at the ending part as gas flows if subsonic and increasing if supersonic. The distance between the nozzle and test section (*L*) is controlled by a micro-scale z-stage attached beneath the test section over the operation range from *0 mm* to *20 mm*. Experiments were performed in the range that are within the operating range of the z-stage, which is a nozzle-to-plate spacing (L/d) of 12.

Figure 3.2(b) shows the details of the test section. Including the copper block, 4 type-T thermocouples, insulation, and silicon heater. Oxygen-free copper with a relatively higher thermal conductivity of *391 W/m-K* than other metals, was chosen as the material for the heated test surface. The dimensions of the copper block are *12.7 mm* × *12.7 mm* × *9.5 mm*, and the thermocouples are inserted at specified locations with cares in treatment. One thermocouple is placed at the center, *0.79 mm*, and the others are *6.35 mm* away from the impinging surface in order for checking radial heat loss and radial surface temperature. Three thermocouples are aligned horizontally at distances of l_1 = *3.25 mm*, l_2 = *2.50 mm*, and l_3 = *0.625 mm*. A silicon heater is attached at the lower surface of the copper block and is connected to a DC power supply. The silicon heater has the same area as the lower surface of copper block so that perfect fit allows that the entire area could be uniformly heated. The ceramic heater was attached to lower surface of the block by Omega bond 200 and corresponding resin. As an electric potential is applied to the heater, Joule-heating is generated by the electric current. The heater has upper limits of *80 V, 26 W, 200 ℃*. Because the thermal conductivity of copper is high, the thermal energy from the silicon heater could be assumed to transfer uniformly and rapidly to the upper surface. The uniformity allows for the consideration of the conduction through the copper block as 1-Dimensional heat flow in the vertical direction. The thermoplastic insulator, which has dimensions of *70 mm* × *70 mm* × *20 mm*, covers the copper block, and both the insulator and the copper block are mounted onto the z-stage, which is vertically movable.

The cooling performances of the N_2 and CO_2 are compared in terms of the surface temperature and surface average heat transfer coefficient in the present study. Assuming a uniform 1-D heat flux with no horizontal thermal spreading, the surface temperatures can be evaluated simply by applying Fourier's law using the measured temperatures and the thermal conductivity of copper. Afterwards, the convective heat transfer coefficients are also obtained from the following relationship, while

considering a reference temperature defined in each experiment,

$$h = \frac{q''}{T_s - T_{in}}. \quad (4)$$

$$h = \frac{q''}{T_s - T_{aw}} \quad (5)$$

Reference temperature was assumed as the nozzle inlet temperature in dry-ice formation experiment, while adiabatic wall temperature is used in supersonic jet experiment. In the former, the inlet temperature which represents the jet fluid before expansion is used in evaluation of heat transfer coefficient. In the latter, the temperature difference in Equation 5 is evaluated by surface temperature and adiabatic wall temperature. The adiabatic wall temperature represents the surface temperature when no power is supplied, so that the temperature is measured when only the effect of the jet bulk fluid exists without the test plate being heated. The copper block is assumed to be perfectly insulated, such that the entire heat flux generated from the heater is dissipated only via forced convection of the impinging jet.

Each of the type-T thermocouples has a maximum error of ± 0.5 ℃. The errors of the electric current and electric potential measured by a DC power supply are ± 0.3 % and ± 0.15 %, respectively. The flow meter has an accuracy of ± 1 % over its full range (0 – 2.6 CFM). The IR camera has an accuracy of ± *1* ℃ or ± *1 %* of reading. The lengths measured by a micrometer have an error of *0.5 mm*. The uncertainties of the heat transfer coefficients calculated from the error propagation by measured variables are shown as error bars in each figure and was less than *5.40 %* in the study.

4. Investigations for Under-expanded Impinging Gas Jet

4.1. Effect of sublimation process

4.1.1. Experimental method

Impinging jet cooling tests were performed under a fixed heating power of *12 W*, which is equivalent to an applied heat flux of *74,511 W/m*^{2}, considering the heating block's surface area. The radial heat loss which bothered assuming 1-D conduction is evaluated later sessions in this paper. To compare both cases of CO_2 and N_2, the data are acquired for values of the nozzle-to-plate spacing (*L/d*) of *5, 10, 15* and *20* and with the volume flow rate fixed at values of 2.36×10^{-4}, 3.30×10^{-4}, 4.72×10^{-4}, 5.66×10^{-4}, and 7.08×10^{-4} m^3/s. In the case of the CO_2 jet, additional experiments for high volume flow rates of 10.38×10^{-4} and 11.80×10^{-4} m^3/s were performed. To normalize the experimental results, the corresponding bulk Reynolds number is defined as

$$Re_d = {\rho V d}/{\mu} \ . \tag{6}$$

The nozzle diameter, which is fixed at *1 mm* in this experiment, is regarded as the characteristic length scale; thus, the velocity can be calculated from the volume flow rate through the tubes. The dynamic viscosity and density of each fluid is obtained in REFPROP [26] by using normal atmospheric conditions of *0.1 MPa* and *296 K*. The resulted Reynolds numbers corresponding to nitrogen has nearly doubled when the parameters switched into the ones of carbon dioxide because of viscosity and density. N_2 jet has its experimental condition from $Re_d = 18{,}405$ to $Re_d = 62{,}577$ and CO_2 jet is from $Re_d = 46{,}174$ to $Re_d = 138{,}521$.

4.1.2. Results and discussion

Figure 4.1 shows the local variation of the surface temperatures and the local heat transfer coefficients of the CO_2 jet with $Re_d = 34{,}692$ calculated with three thermocouple data in the copper block. The variation of the local surface temperature and local heat transfer coefficient between three points is trivial compared with the variation between the different nozzle-to-plate spacing values. The maximum difference of three surface temperatures is *0.51 ℃*, and that of the three local heat transfer coefficients is *11.9 W/m*^{2}*-K*. These radial temperature differences may cause radial heat losses. The heat losses are evaluated using measured points distances l_1 and l_2. The maximum radial heat loss is evaluated as *2,201 W/m*^{2} at *L/d = 5*, which is *2.95 %* of the main heater surface normal direction heat flux, which is possibly negligible in the main heat flux evaluation, but they are

included as an uncertainty of heat flux. Detailed data are shown in Table 4.1. With minor variation of radial temperatures distribution, the surface temperature and surface heat transfer coefficient can be characterized by the stagnation temperature and average heat transfer coefficient. As the nozzle-to-plate spacing is varied over 5 increments from *L/d = 5*, the temperature increments are *3.1 ℃*, *3.2 ℃* and *3.9 ℃* in order and the local variation of the surface temperature is *13.1 %* of the temperature increment. Because of the high thermal conductivity of copper, the conduction through the copper block is considered to be uniform and 1 dimensional normal direction to the cooling surface. The local variation can be neglected, as previously stated.

Following experiment is for Joule-Thomson effect of each gas. Expansion process through nozzle orifice into the ambient air should come with pressure drop, resulting bulk-jet fluid's temperature decrease. Figure 4.2 shows the measured nozzle inlet temperature and nozzle exit temperature of the CO_2 jet when the Reynolds number is *230,869***.** The CO_2 jet is ejected through the converging nozzle with a drastic temperature drop due to the Joule-Thomson effect. In this experiment, the formation of dry-ice particles is observed in naked eye. The pressure of the nozzle inlet is measured as *1,797 kPa*, and the pressure of the nozzle exit is assumed to be equal to atmospheric pressure, that is, *100 kPa*. With an under-expansion ratio of *18*, the temperature decreases from *-22.06 ℃* to *-34.77 ℃*. In Figure 4.2, the stagnation temperature of the target surface is assumed as the nozzle exit temperature when the heat flux is not applied. The surface stagnation temperature is measured from the thermocouple measurement in the copper block because the surface temperature of the copper block reaches equilibrium with the jet fluid. The effect of expansion through the nozzle tends to be increased as the Reynolds number increases. However, the measured values of the nozzle exit temperature for all cases are not low enough to form dry-ice particles at atmospheric pressure, even though the dry-ice particles formed after the expansion are visually observed for those all cases. This discrepancy is caused by the reasons that the heat transfer between the bulk jet fluid and ambient air could not be prevented and heat transfer between the surface of the heater block and ambient air also occurs. In the present study, because the CO_2 source is limited in its ability to maintain a high Reynolds number, all experiments had been performed with a Reynolds number of less than *230,869*.

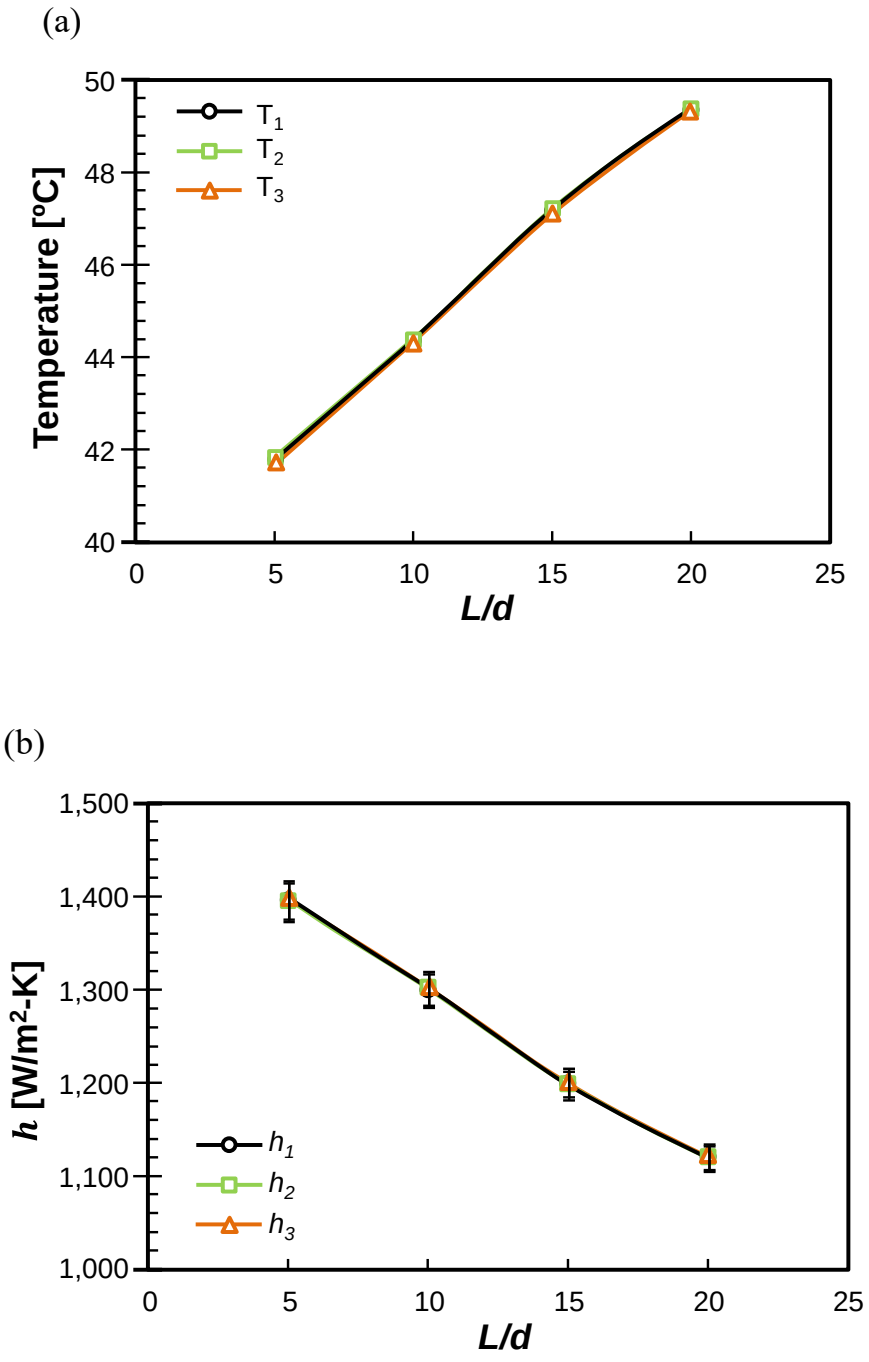

Figure 4.1. Local variation of surface temperatures and local heat transfer coefficients of CO_2 jet flow with $Re_d = 46,174$

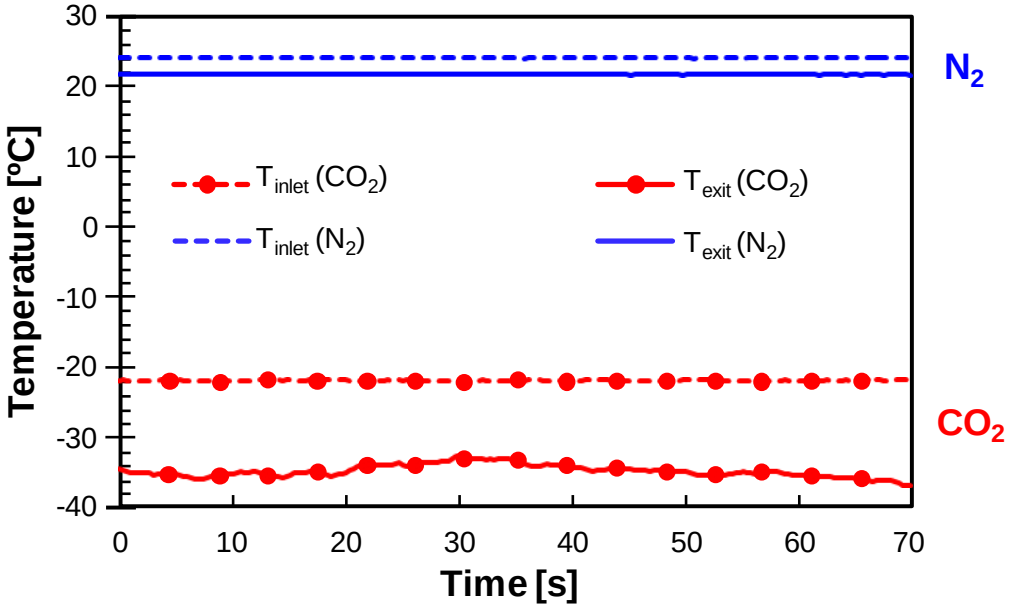

Figure 4.2. Jet nozzle temperature variation by N_2 (Re_d = *62,577*) and CO_2 (Re_d = *230.869*) expansion

Table 4.1. Radial heat loss evaluated by thermocouple measurements

L/d	T_1 [K]	T_2 [K]	T_3 [K]	q_{loss}"(T_1-T_2) [W/m2]	q_{loss}"(T_2-T_3) [W/m2]
5	43.13	43.06	42.92	**790.238**	**2200.78**
10	45.73	45.66	45.56	**869.488**	**1591.96**
15	48.52	48.44	48.31	**912.753**	**1982.26**
20	50.71	50.62	50.55	**1095.28**	**1035.54**

Then, the experiments changing the nozzle-to-plate spacing and Reynolds number were carried. Figure 4.3 shows the measured stagnation temperatures and average heat transfer coefficients of the CO_2 jet when a power of *12 W* is applied. Varying the nozzle-to-plate spacing causes temperature and convective heat transfer coefficient changes. The relationship between the nozzle-to-plate spacing and heat transfer coefficient was also investigated by Lee and Lee [30]. In this study, the stagnation temperatures are increased almost linearly as the nozzle-to-plate spacing increases. The stagnation temperature with $L/d = 5$ and $Re_d = 138{,}521$ is *13.9 ℃*; this temperature is different by *17.1 ℃* compared with the temperature with $L/d = 20$ of *31.0 ℃* for the same Re_d. The temperature differences between $L/d = 5$ and $L/d = 20$ have the same trend with various Reynolds numbers, resulting in similar slopes of each case. Related to the increasing stagnation temperature, the heat transfer coefficients decrease with the nozzle-to-plate spacing instead. Unlike the stagnation temperatures, the heat transfer coefficients have a large difference as the nozzle-to-plate spacing becomes smaller.

This trend is applicable to the N_2 jet as well, as shown in Figure 4.4. The N_2 jet experiment is performed with lower Reynolds numbers than those of the CO_2 jet, because the N_2 source has a limit in its pressure, resulting in higher stagnation temperatures. However, the values of the average surface heat transfer coefficients from N_2 jet test are relatively comparable to those of CO_2, as shown in Figure 4.3(b) and Figure 4.4(b). The heat transfer coefficients of N_2 show less sensitive change to the change of L/d even at a high Reynolds number and a small nozzle-to-plate spacing, unlike the outputs from CO_2 tests. This result is considered due to the difference between the single-phase jet and the solid-gas two-phase jet. With higher Reynolds number of CO_2 jet flow, more dry-ice particles formation are expected, since more pressure expansion or larger pressure drop occur during passing through the jet nozzle.

The effect of the Reynolds number with CO_2 jet is represented in Figure 4.5. A high Reynolds number corresponds to not only a higher gas flow but also to a higher nozzle inlet pressure, resulting in a higher pressure drop when gas is expanded through the nozzle. A larger amount of CO_2 with a lower temperature is guaranteed by the Joule-Thomson effect as the gas passes through the nozzle and impinges the target surface. Namely, a high Reynolds number improves heat transfer between the flow and target surface, such that the stagnation temperature decreases, as shown in Figure 4.5(a), and the heat transfer coefficient increases, as shown in Figure 4.5(b). With a short nozzle-to-plate spacing, such as $L/d = 5$, the Reynolds number has a great influence on the heat transfer coefficient, while the heat transfer coefficient shows less change if the nozzle is far away from the test section, such as $L/d = 20$. In addition, as the Reynolds number becomes higher, the heat transfer coefficients tend to be rapidly increased. These phenomena are explained that higher Reynolds number and higher pressure drop bring about more dry-ice particle formation.

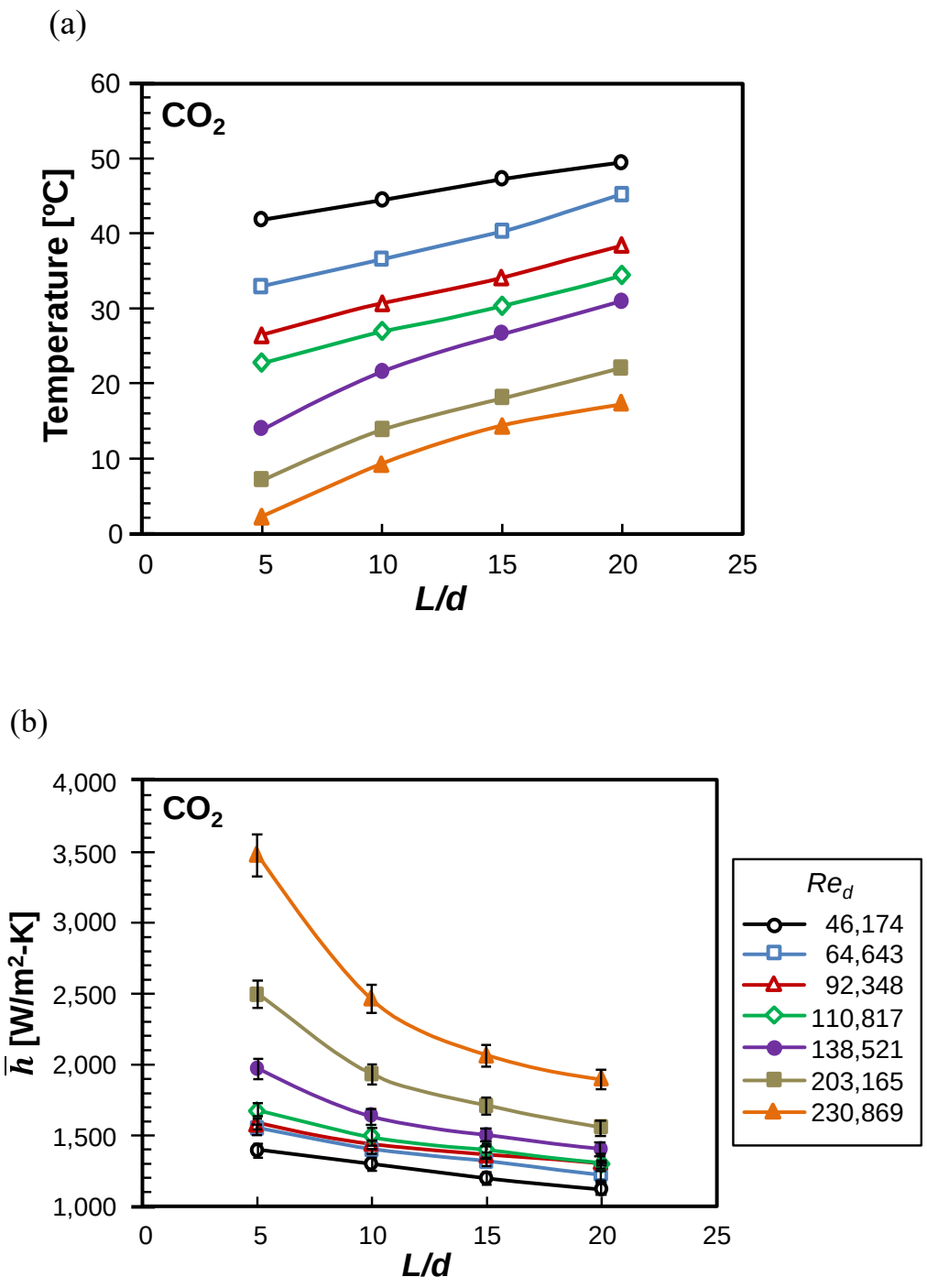

Figure 4.3. (a) Stagnation temperature and (b) surface average heat transfer coefficient of CO_2 jet flow with various *L/d* (error bars indicating the measurement uncertainties)

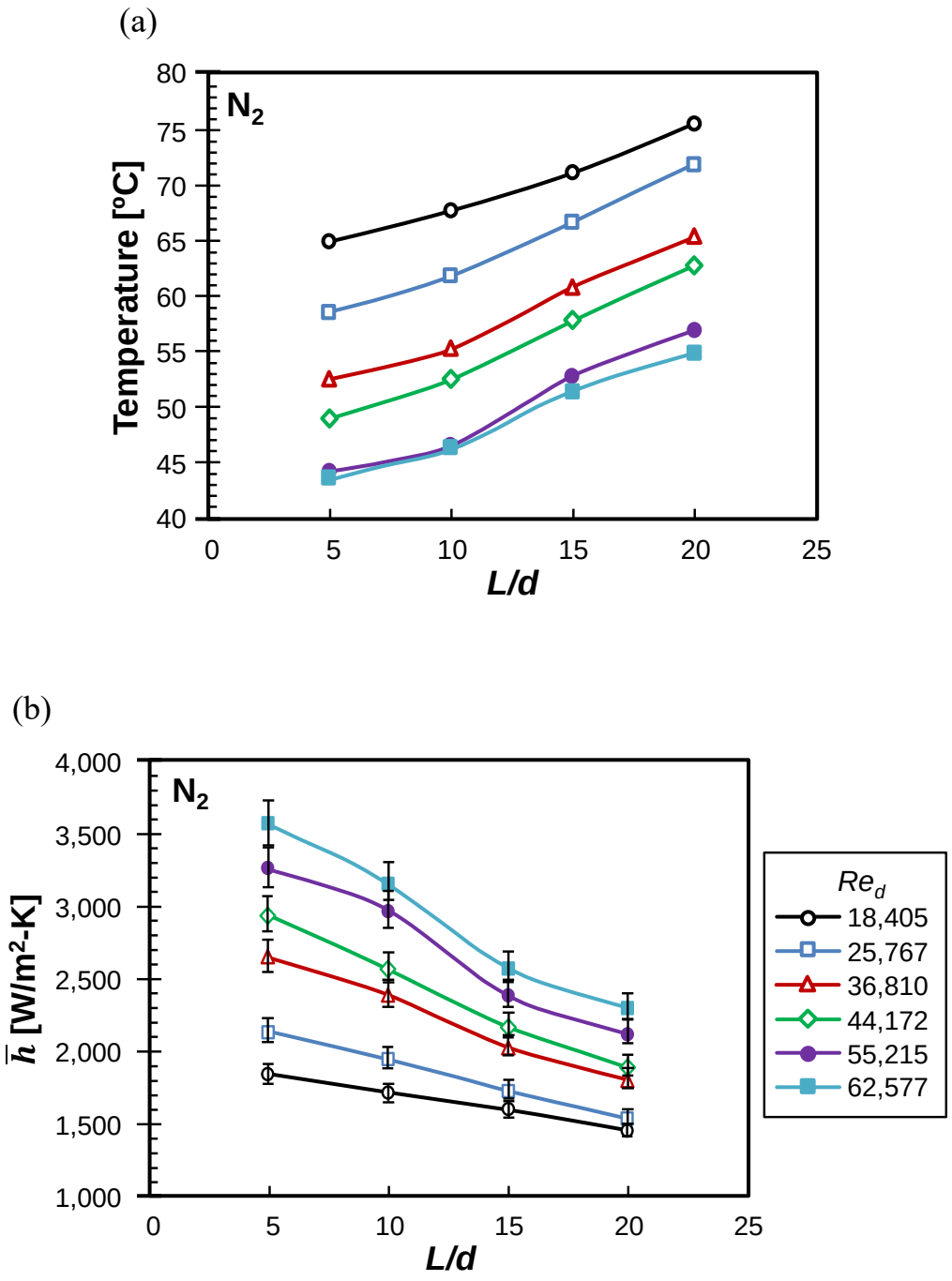

Figure 4.4. Stagnation temperature and (b) surface average heat transfer coefficient of N_2 jet flow with various *L/d* (error bars indicating the measurement uncertainties)

For the conditions of the *12 W* power supply and *L/d = 5* and *10* ratio, the stagnation temperatures and average convective heat transfer coefficients of CO_2 and N_2 are compared in Figure 4.6. Figure 4.6(a) shows that the stagnation temperature of CO_2 is lower than that of N_2, if the two flows have the same Reynolds number. Around $Re_d = 45{,}000$, the CO_2 jet causes *8.1 ℃* lower stagnation temperature than that of N_2 jet. This amount of temperature difference could be achieved by nearly doubling the Reynolds number for the N_2 jet from $Re_d = 25{,}767$ to *44,172*. This trend clearly shows that the CO_2 jet effectively achieves lower surface temperature than the N_2 jet. Nonetheless, Figure 4.5(b) shows the average heat transfer coefficient of the CO_2 jet is lower, despite the cooling performance being superior to that of N_2. For the heat transfer coefficient evaluation in Equation (4), the nozzle inlet temperature is used as a reference. Because the nozzle inlet temperature of the CO_2 jet is from *-11.1 ℃* to *-21.9 ℃*, which is far lower than that of N_2 at *23.8 ℃*, the average heat transfer coefficient of CO_2 tends to be under-estimated. The temperature of ambient air is quite close to the nozzle inlet temperature of the N_2 jet and is far above from the temperature of the CO_2 jet. As a result, the heat transfer between the bulk jet fluid and the ambient air accounts for a much smaller percentage out of the entire heat transfer amount in the case of the N_2 jet compared to that of the CO_2 jet. This difference is difficult to be identified in the calculation. However, in the case of a high Reynolds number, such as *203,165* and *230,869*, the average surface heat transfer coefficient rapidly increases. The heat transfer coefficient of the CO_2 jet eventually reaches the coefficient of the N_2 jet and then exceeds it, despite the under-estimation. This phenomenon can be explained by including the sublimation process of the dry-ice particles formed in the conditions of a high Reynolds number, resulting in better cooling performance.

Figure 4.7 compares the temperature distribution of the copper block's surface obtained by an IR camera imaging. To synchronize the IR temperature reading and the thermocouple stagnation temperature measurements, the emissivity of copper block's surface is adjusted in the range of *0.18 – 0.20*. With *L/d = 10* fixed, the temperature distribution for 2 different Reynolds number of *36,810* and *48,569* are captured in each case. For CO_2 jet in these Reynolds number range does not experience enough pressure drop to form noticeable amount of dry-ice particles. However, these range were chosen for CO_2 flow to be matched with the comparison counterparts, N_2 jet which has upper side Reynolds number limitation. The temperature range is synchronized as being equal from *20.0 ℃* to *80.0 ℃* to identify the temperature difference between them. With a Reynolds number of *36,810*, the

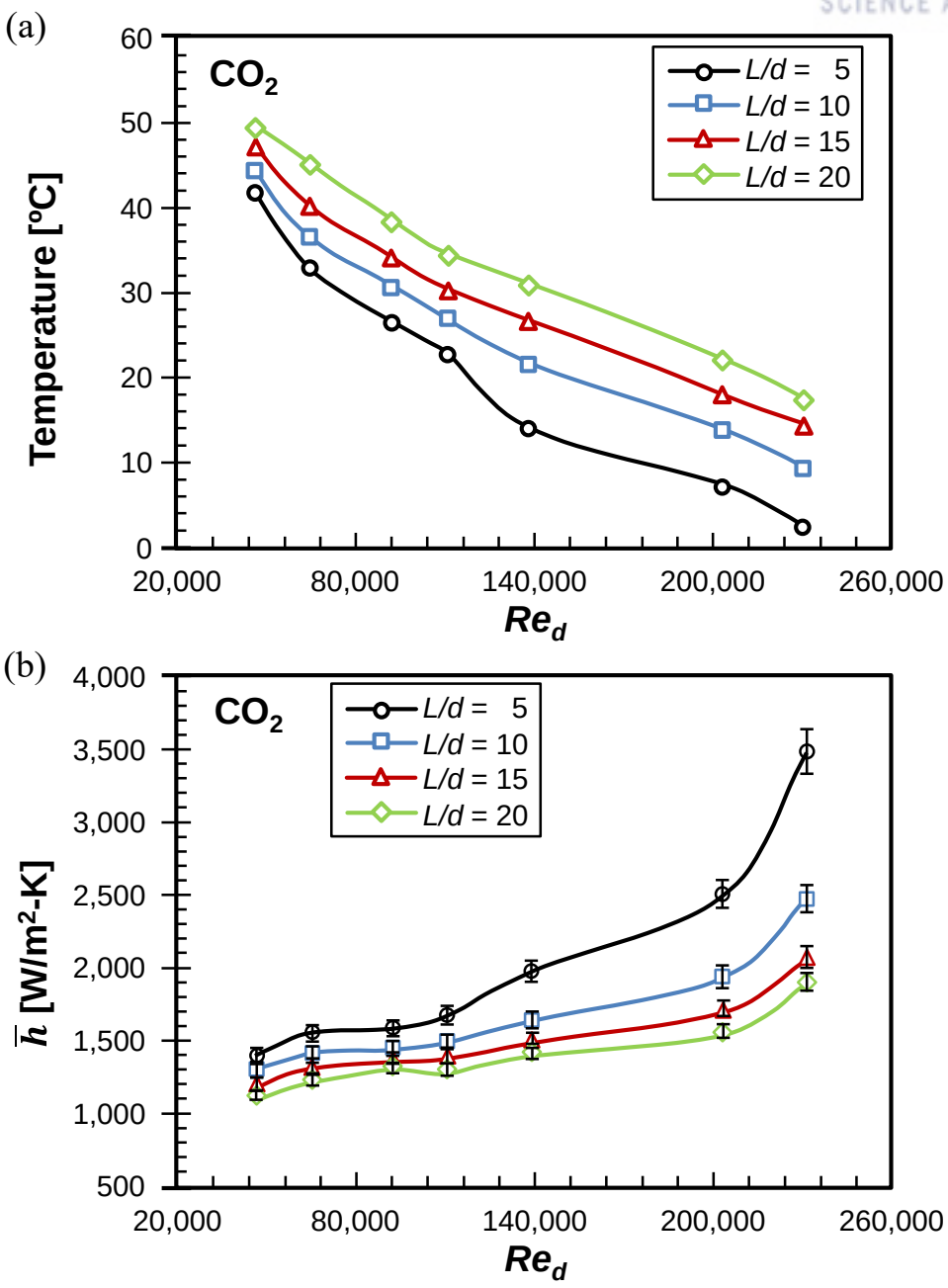

Figure 4.5. (a) Stagnation temperature and (b) surface average heat transfer coefficient of CO_2 jet flow with various Reynolds number (errors bar indicating the measurement uncertainties).

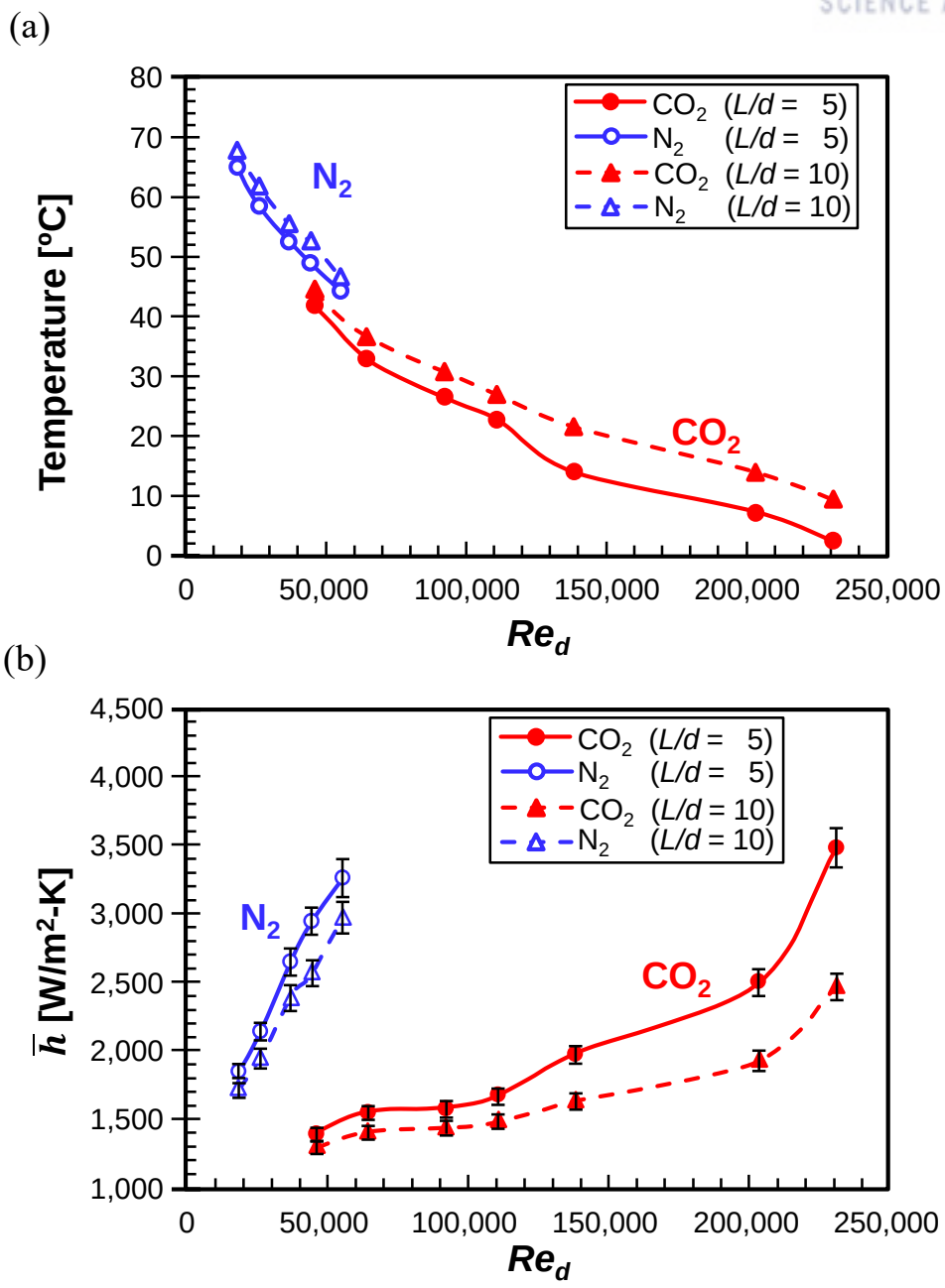

Figure 4.6. Comparison of (a) stagnation temperature and (b) surface average heat transfer coefficient between N_2 and CO_2 with L/d = 5, 10 (error bar indicating the measurement uncertainties).

stagnation temperature of the CO_2 and N_2 jet is *44.2 ℃* and *54.8 ℃*, respectively**.** For each data point, the symmetry about the vertical direction is broken because the captured angle is tilted; thus, only the horizontally distributed temperature needs to be considered. The center stagnation temperature is the lowest temperature out of the surface temperatures, and the temperature tends to increase with distance from the stagnation point in the case of CO_2 jet, whereas the surface temperature of N_2 jet has relatively uniform distribution. Joule-Thomson coefficient of CO_2 jet, which is much higher than the one of N_2 jet, affects the instantaneous stagnation temperature drop. In both jets, the temperature decreases as the volume flow rate or Reynolds number increases. The surface temperature is lower with the case of the CO_2 jet, if the Reynolds number is the same, that is, a better cooling performance is observed in the case of the CO_2 jet. The IR camera parameters, such as emissivity and reference temperature, were properly adjusted, calibrated with the thermocouple measurement data.

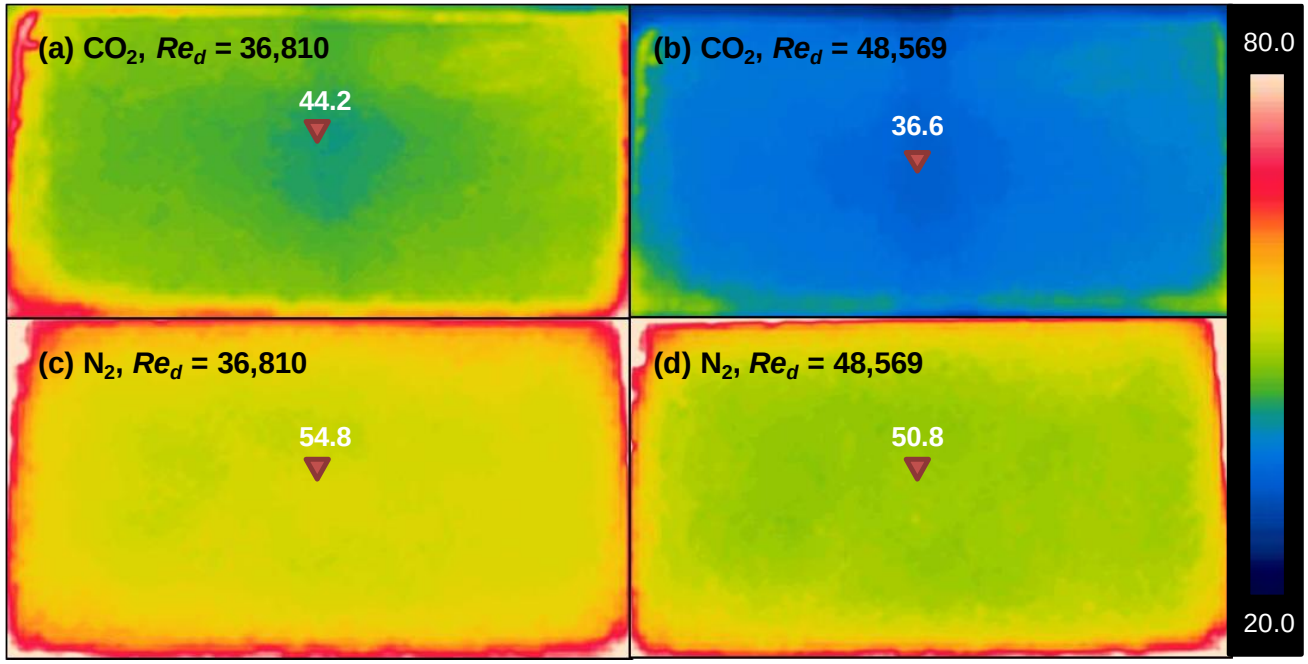

Unit: [ºC]

	Case	Stagnation Temperature [ºC]
CO_2	(a) Re_d = 36,810	44.2
	(b) Re_d = 48,569	36.6
N_2	(c) Re_d = 33,129	54.8
	(d) Re_d = 47,853	50.8

Figure 4.7. Temperature distribution of copper block top surface captured by IR imaging

4.2. Effect of jet flow structures

4.2.1. Experimental method

Table 4.2 shows the nozzle pressure ratio (NPR) used in the present study and the corresponding Reynolds number, mass flow rate and Mach number. The NPR in this study is defined as the ratio of two pressure values, using the ambient pressure of 101.3 kPa and the nozzle inlet pressure, instead of the ambient pressure and nozzle exit pressure. This is because of the difficulty in measuring the nozzle exit pressure with the tiny nozzle diameter of the present experiment, 1.5 mm. Possibly the pressure probe tip may disturb the flow and the pressure measurement be affected. The detecting problem arises because probe tip size is more than *30 %* of nozzle diameter. The Reynolds number is also defined as stated previous discussion, where the dynamic viscosity and the density, properties of nitrogen used in the equation, are all obtained in REFPROP [13] by using ambient temperature and pressure of *101.3 kPa* and *298 K*, respectively.

The speed of sound and the Mach number is calculated using the ambient temperature of 298 K and the gas constant of nitrogen, 1.4. The resulting speed of sound in nitrogen gas is 351.9 m/s. The jet downstream flow of NPR = 2 is the only case in the subsonic region, and all of the other cases are in the supersonic region. NPR = 2, 3, 4, and 5 correspond to Mach numbers of 0.89, 1.17, 1.52, and 1.87, respectively, and the transition occurs at NPR = 2.71. In the present experiments, the NPRs are set from 2 to 5 with an interval of 1, which covers not only a moderately under-expanded but also a highly under-expanded region. The compressibility effects are dominant as the NPR becomes higher, so that more complex and stronger shock structures could be obtained.

The flow visualization tool chosen in this experiment is a schlieren imaging system as stated in the previous section. In PIV (Particle Image Velocimetry) methods, working fluids are seeded using tracer particles such as one-half micron alumina particles and laser illuminate the particles into visible. This method provides accurate velocity profile with large vortices cascading away from the stagnation point and jet boundaries, however, it couldn't catch up the shock cell structures. On the other hand, with a high-speed camera (Phantom ES-200), the jet flow structure could be captured by using a one-mirror system. Figure 4.8 represents the schlieren system used in this experiment. All the components of the system including the camera, knife edge, beam splitter and mirror, are aligned carefully to obtain shadowgraph images. Light is supplied from the light source which is equipped right above the beam splitter, and then propagated to the mirror after being reflected by the beam splitter. Then, after the light is reflected by the mirror, it regresses to the beam splitter and then passes through the beam splitter toward the knife edge and the camera. The right and left side edges of the focused light are cut by the knife edge, causing a refraction effect of the light, then, the nearby ambient air's minor

movements and shock structures inside the jet boundary could be depicted as shadows. Finally, the image processed by all of the schlieren components is recorded by the high-speed camera sensor.

Considering the configurations of the experimental apparatus, a mirror with a focal length of *305 mm*, a camera lens with *200 mm* and pin hole of *200 um* are chosen in the present study. The schlieren system occupies *710 mm*, which is approximately two times the mirror's focal length. For the light focusing on the camera, it should pass the mirror's focal length twice. The distances between each component are carefully fixed based on the mirror's focal length, as represented in Figure 4.8.

$$\frac{1}{f} = \frac{1}{D_o} + \frac{1}{D_i} \tag{7}$$

Equation (7) is a formula for setting up the schlieren system in present study. The focal length of the mirror (f) affects the other factors Do and Di, which are the distances between the knife edge and beam splitter and the mirror, respectively. As the schlieren system in this experiment is a one-mirror system, Do and Di might have similar values because the knife edge and beam splitter are located close together.

The high-speed camera is capable of storing a data stream of up to 4 GB, which is related to its resolution and capture speed. A resolution of 1280 pixels × 800 pixels and a capture speed of 300 fps, which are enough to capture the flow structure under the present experimental conditions, are chosen in this experiment. The camera is able to capture an instant, but the jet flow structure does not need to be captured at every instant because the flow structures are in the steady state, so only a stationary image is captured under each experimental condition.

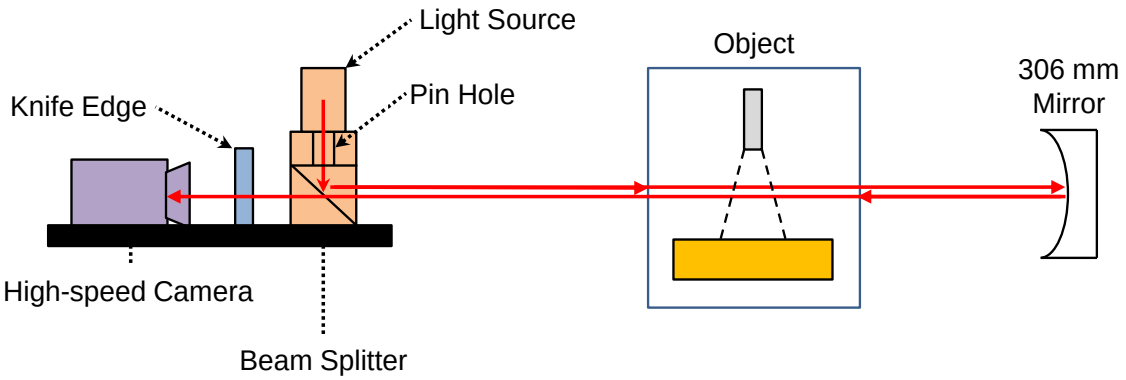

Figure 4.8. Schematic of one-mirror Schlieren system

Table 4.2. Nozzle pressure ratio and corresponding flow characteristics in each experimental case

NPR	2	3	4	5
Re_d [-]	30,068	39,751	51,687	63,402
$\dot{V}$ [m^3/min]	0.033803	0.043737	0.056869	0.069759
M [-]	0.887	1.172	1.524	1.870

Impinging jet cooling tests were performed under a fixed heating power of *18 W*, which is equivalent to an applied heat flux of *110,461 W/m*^{2}, reflecting the heating block's surface area. The surface temperature is measured both when no heating power is applied (T_{aw}) and when heating power is applied (T_s). The data are acquired for values of the nozzle pressure ratio (*NPR*) from 2 to 5, to study the effect of the nozzle geometry and jet fluid's volumetric flow rate. The nozzle diameter, which is fixed at *1.5 mm*, is regarded as the characteristic length scale; thus, the velocity can be calculated from the volumetric flow rate through the tubes.

4.2.2. Results and discussion

At first, shadowgraphs of both N_2 jet and CO_2 jet have been obtained and resulted pictures are shown in Figure 4.9. Experiment of N_2 jet was performed in conditions of Re_d = *63,402* (*NPR = 5*) while the experiment of CO_2 jet was performed with Re_d = *203,165* (*NPR = 14.0*). Nozzle pressure ratio is regarded as an indicator of under-expansion. Thus, higher NPR experiences severe under-expansion and clearer shock structures at jet downstream, not to mention that has higher jet fluid velocity as well. However, CO_2 jet performed in this experiment represented few shock cell even though fluid Mach number exceeded 2.0. Jet boundaries of CO_2 jet has thicker layer than the boundaries of N_2 jet as well. The main differences are caused by fluid velocity of each gas. If the same Mach number was set in both jets, Reynolds number of bulk CO_2 jet fluid is much larger than N_2 jet's. Jet fluid velocity differences are related to total pressure at the jet boundaries, making the layers thicker as shown in Figure 4.9(b). By this mean, Schlieren shadowgraph captures different flow structures at jet downstream of each jet, and the shock cells of CO_2 jet were diminished despite of its highly under-expanded experimental condition. Namely, N_2 jet has much benefits comparing with CO_2 jet in the sense of flow visualization because shock structures of N_2 jet is more clearly captured in same condition, which is convenient to control flow rate and the requirements are easy to achieve due to properties of N_2 such as viscosity and specific heat ratio. N2 is selected as working fluid and the following experiments about supersonic jet investigations were performed only on N_2 jet as stated previously.

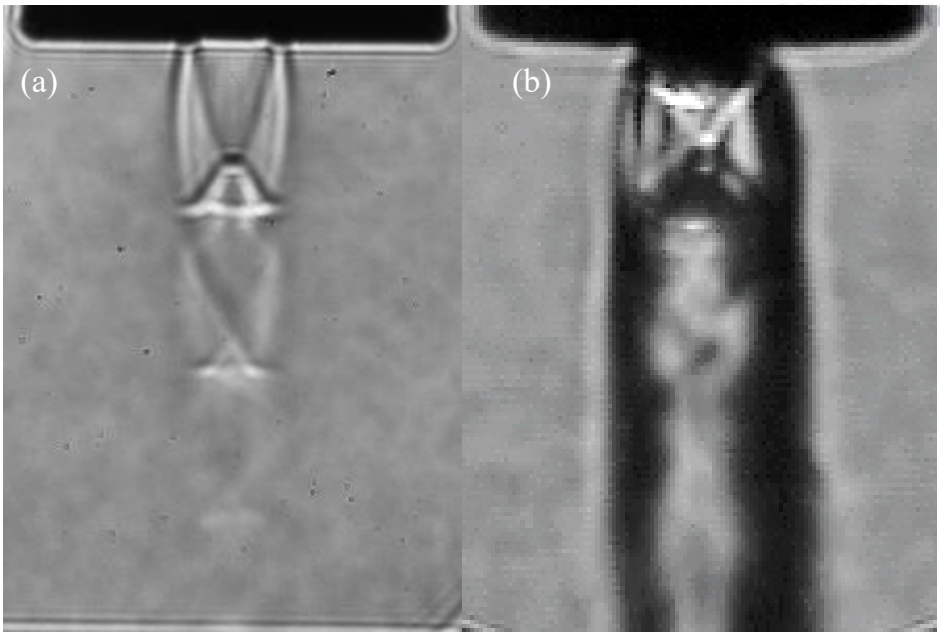

Figure 4.9. Jet structures of (a) N_2 jet and (b) CO_2 jet

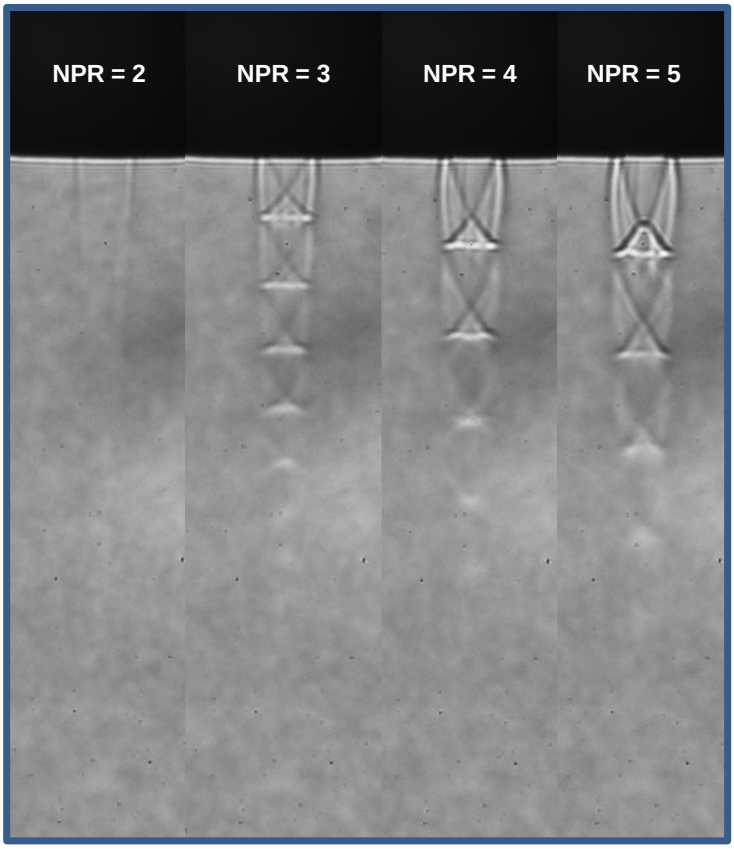

Figure 4.10. Flow fields of free-jet stream captured by Schlieren system

Figure 4.10 shows the flow field structures of the free-jet for each NPR. After the jet flow is ejected at the nozzle outlet, a shock structure and jet downstream propagation can be seen in this figure. The first case with *NPR = 2* has no shock structures unlike the other cases because it does not exceed the transition condition of *NPR = 2.71*. Therefore, the jet boundary between the ambient environment and jet flow is dimly captured and soon vanishes. The other cases, NPR = 3, 4, 5, have flow structures as shown in **Figure 1(a).** The core boundary, oblique shock and reflected shock structures are constructed on the jet downstream. As the pressure ratio increases, the compressibility effects of the jet flow become magnified. For example, the Mach number of each experiment increases or these shock cell structures become stronger and longer, resulting in clearer images being captured. In each experimental case, the jet flow velocity, which is definitely supersonic except in the case of NPR = 2, is lowered as it experiences many shocks during propagation and loses the original momentum it contained at the nozzle exit. The supersonic core length, which is defined as the distance until the jet centerline velocity becomes subsonic, is nearly located at *L/d = 10* in this experimental condition, though the pressure ratios are different [31]. This tendency is also represented in Figure 4.10.

Figure 4.11 presents the adiabatic wall temperatures and stagnation temperatures with Q = 18 W applied. The nozzle-to-plate distance (L/d) controlled by the micro-stage is responsible for the surface temperature changes, although temperature fluctuations are captured in most experimental cases instead of a monotonic increase. Though the low pressure ratio shows a monotonic increase, the fluctuating phenomenon, which has never been mentioned before, arises only in the supersonic flow region (NPR = 3, 4, 5). After the transition at NPR = 2.71, the adiabatic temperature at a low distance suddenly drops from 21.8 ℃ to 17.6 ℃, as shown in Figure 4.11(a). Compared to the ambient temperature of 24.5 ℃, the target surface cools down in adiabatic conditions, but the cooling performance fluctuates when L/d changes. Larger peak-to-valley temperature differences are measured when a high pressure and high jet velocity are supplied, reaching a maximum difference of 3.6 ℃ in the case of NPR = 5. The fluctuations exist only between L/d = 4 and L/d = 10. The main reason for the temperature fluctuations is related to the shock structure seen in shadowgraphs. The momentum carried by the jet fluid also affects the result. If the jet fluid flows away enough to be out of the supersonic core length, the jet flow becomes subsonic, and the compressibility effects, including the temperature fluctuation, are rapidly diminished. These trends have been observed in surface heating conditions as well (Figure 4.11(b)). Due to heat flux from the ceramic heater, the stagnation temperature experiences great increases in all cases. Temperature fluctuations are also found in the supersonic region, with slightly greater peak-to-valley differences than those under adiabatic wall conditions, with value of 4.4 ℃ versus 3.6 ℃, as shown in Figure 4.11(a) and 4.11(b), respectively. . The nozzle-to-plate distance where the temperature climbs and dives is identical in all

experimental cases. As an example, the temperatures of NPR = 5 are compared in Figure 4.12. Though tiny mismatches occur at low L/d, the data points from the main temperature-changing region from L/d = 4 to L/d = 10 are identical in both conditions, and the result is obtained repeatedly at least twice. Shock structures that are not affected by the heat flux cause the fluctuations in the cooling performance, and this phenomenon commonly occurs in all experimental cases except for NPR = 2.

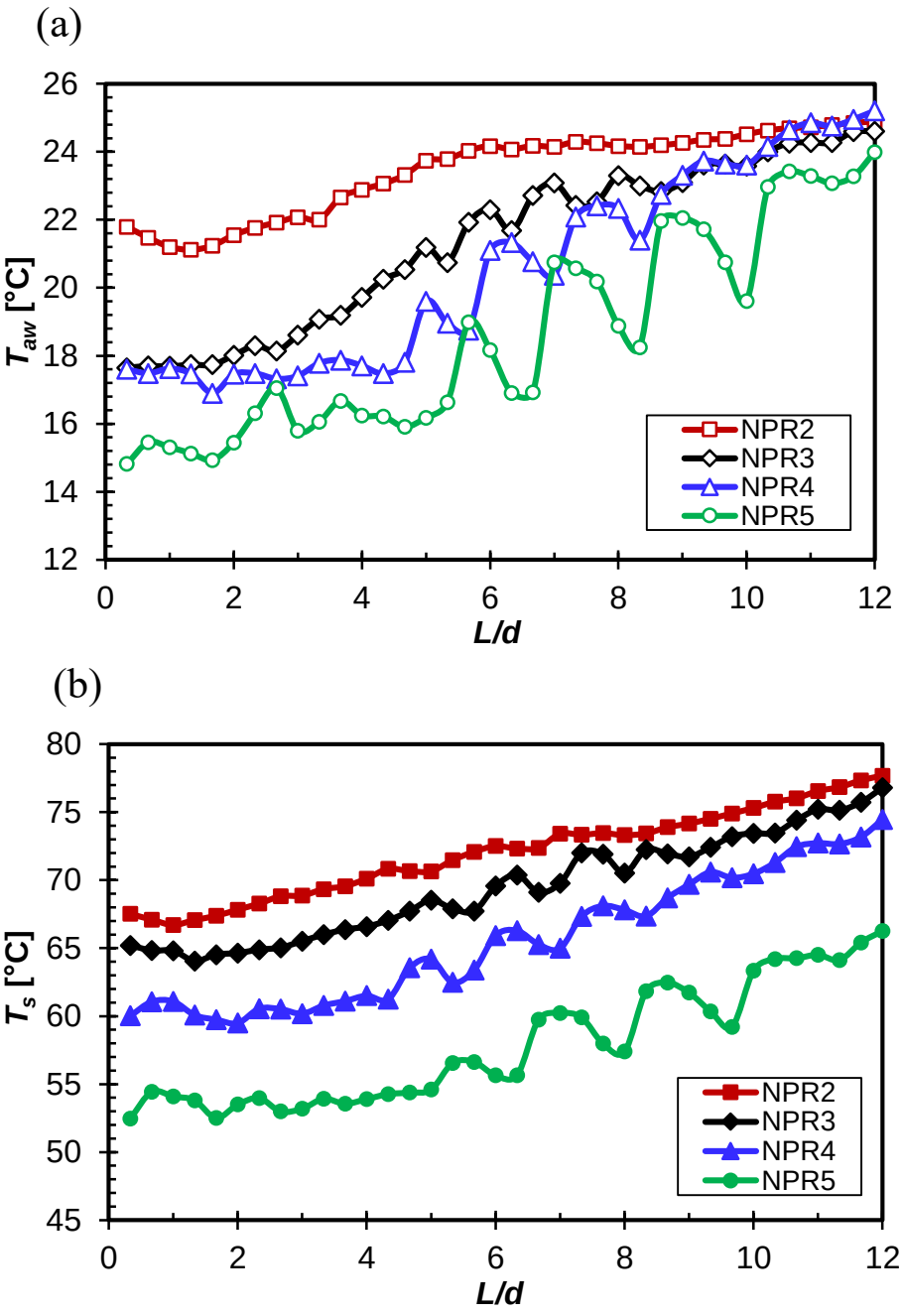

Figure 4.11. (a) Adiabatic wall temperature and (b) stagnation temperature with *Q = 18 W*

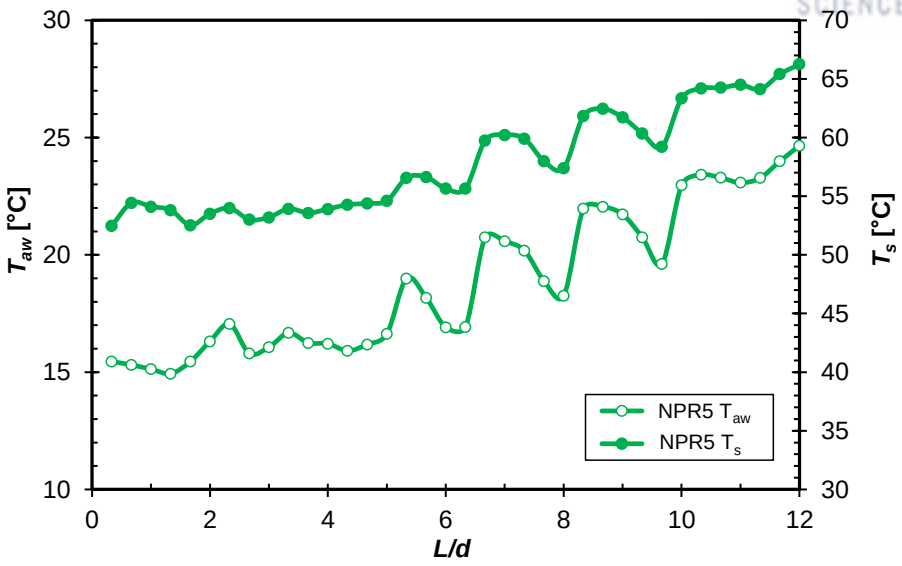

Figure 4.12. Adiabatic wall temperature and stagnation temperature with *Q = 18 W, NPR = 5*

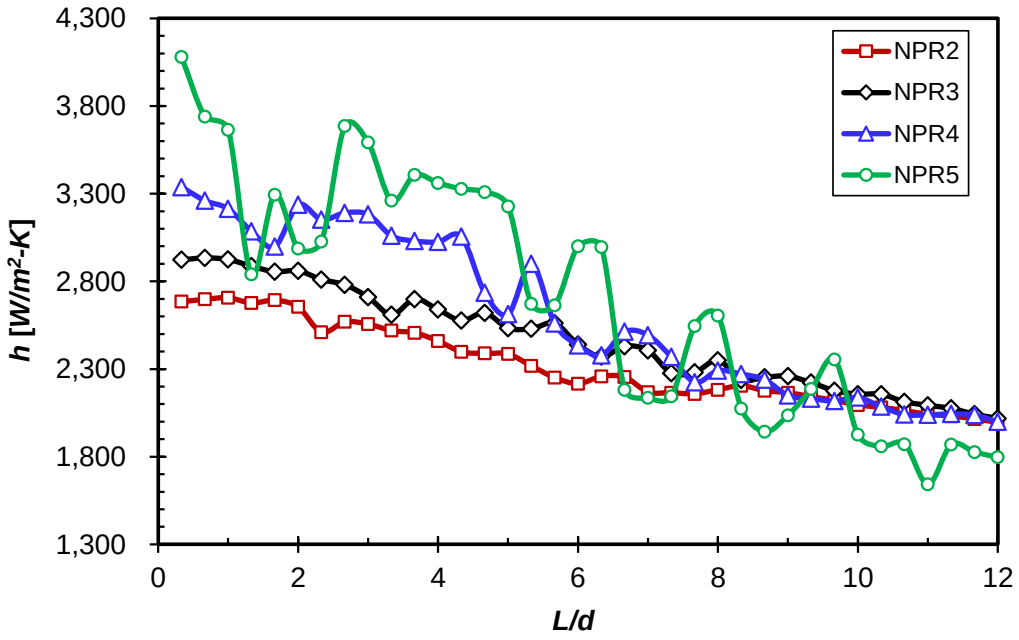

Figure 4.13. Surface average heat transfer coefficient with the nozzle of 1.5 mm diameter

The cooling performance at the target surface could be represented as the surface average heat transfer coefficient, as shown in Figure 4.13. Three surface temperatures are calculated from the thermocouple measurements shown in Figure 4.11(b) and averaged to evaluate heat transfer coefficient. As a result, the surface temperature difference affects the heat transfer, as expected. The heat transfer coefficient eventually reaches a saturation point at higher L/d, while it varies greatly at lower values of L/d. As the nozzle-to-plate distance decreases, the heat transfer coefficients are sensitive to the temperature differences between the conditions of adiabatic wall and heating, so that the peak-to-valley difference reaches 824 W/m^2-K out of 3664 W/m^2-K in the case of NPR = 5. That is because temperature difference is divided in evaluating heat transfer coefficient. Flapping on temperature at closer position has resulted huge amount of fluctuations in heat transfer coefficient, which is maximized at *L/d = 1.0* and *1.3* with *NPR 5*. The trend of fluctuation amplified with increasing NPR indicates that the fluctuation is expected to be intensified if under-expansion ratio gets more severe.

Figure 4.14 to 4.17 are data sets of surface temperature measurements and schlieren shadowgraph in each experimental case with nozzle-pressure ratio (*NPR*). Shadowgraphs of each figure correspond to the key temperature climbs or drops that are marked in the plots. Shadowgraphs are obtained between L/d = 2.0 and L/d = 8.0 because of an alignment problem in the schlieren system, which means that misfocusing occurs if the distance between the nozzle and plate is too great.

Figure 4.14 represents the only subsonic case in this study, *NPR = 2*. The temperature increases monotonically and has nearly no fluctuation in the entire domain that this study investigated. In the corresponding shadowgraphs, no shock structure was obviously observed as well. The jet boundaries are dim and disappear quickly, so the structure of the impinging jet is almost the same as that of the free jet in Figure 4.10. Even after transition, *NPR = 3* has nearly monotonic increases in the surface temperature, as shown in Figure 4.15(a). The shadowgraphs in Figure 4.15(b) have shock structures, such as oblique shock, reflected shocks and Mach disks with core boundaries. Several oscillations in temperature are captured by the thermocouples, and the shock structure differences between the peaks and valleys were captured by the schlieren system. This trend can be observed more clearly as a larger pressure ratio, shown in Figure 4.16 and 4.17. The moderately under-expanded case is *NPR = 4* as shown in Figure 4.16. The surface temperatures have four fluctuating cycles, which can be represented by the jumping points L/d = 4.6, 5.6, 7.0, 8.3. These points are captured in shadowgraphs as Figure 4.16(b) shows. The main difference between the peaks and valleys is the relative positioning of the target surface with respect to the flow shock structure. In one shock cell, oblique shock exists in the jet boundary, and the shock is gathered to a Mach crossing point and then reflected so that reflected shocks are constructed continuously. When local minima

occur, the target surface is located on oblique shocks slightly above the Mach crossing point, while local maxima occur when the target surface is put on reflected shocks beneath the Mach crossing point. The former includes cases③, ⑤, and ⑦, and the latter represent cases④, ⑥, and ⑧. Additionally, if the target surface goes down through the crossing point, the jet boundaries become slightly faint and the shock cell length is decreased as well. This phenomenon is caused by the recirculating flow directions after the oblique shock and after the reflected shock that are radially reversed, in the author's opinion. As L/d exceeds 10, the jet flow becomes subsonic so the temperature data and shadowgraphs have monotonic results as in cases with a lower pressure ratio. In Figure 4.17, the condition is on highly under-expanded as pressure ratio increases. The magnitude of temperature fluctuation is much larger and shock cell length becomes longer as well. As shown in Figure 4.17(b), the location of the target surface matters at the cooling performance of the stagnation point, as previously stated. The Mach disk and subsonic slip line appear at the first shock cell on the strength of the high NPR, but the pressure is reduced during some shocks and the jet flow has moderately under-expanded flow structures. The case of NPR = 5 also has four temperature-fluctuating cycles, and the corresponding shadowgraphs are well matched with them. The shock cells in Figure 4.14(b) to 4.17(b) become clearer and larger, which is supported by temperature measurements. As the shock cells get larger in size, the count of clear fluctuations is originally 4 data points with NPR = 3, but is 5 data points with NPR = 4 and 6 data points with NPR = 5 for the second cycle view. Additionally, the starting point of the fluctuation is located at a distance from the nozzle exit, with L/d = 4.3, 4.6, and 5.3 for NPR = 3, 4, and 5, respectively.

The main difference between the peak and valley is the flow direction at the stagnation point as shown in Figure 4.18. As shown in Figure 1.2(b), recirculating flow occurs in an impinging jet. In this study, supersonic shock structures affect the flow direction in different ways according to the location of the impinged surface. Relative location of target surface to the shock structure determines the direction of the flow. If the surface is located before the crossing point, Figure 4.18(a) shows that the jet fluid directly flows away from stagnation to the wall-jet region, so that recirculation flow barely occurs and the fluid is smoothly eliminated. In this condition, the cooling performance is magnified. In contrast, the jet fluid through reflected shock tends to flow toward the stagnation point if the surface is located under the crossing point, as shown in Figure 4.18(b). The lowered jet centerline velocity allows the nearby flows to recirculate, so the jet flow is gathered and is partially trapped at the stagnation, which makes the cooling performance gradually worsen. The result appears as temperature data fluctuations and shadowgraph images, as Figure 4.14 to 4.17 show. The temperature fluctuations do not appear at low L/d because the jet momentum is not reduced yet. The high momentum retained during early expansion keeps the centerline velocity high, which recirculating flow would not allow even if the impinged surface is on the reflected shock. On the other

hand, when the jet momentum becomes gradually reduced during the experiences of several shocks at high L/d, the jet flow always propagates away from the stagnation point, and there is no recirculating flow allowed. Hence, the existence of recirculating flow affects heat transfer, and the location of the impinged surface is dependent on the cooling performance of the supersonic impinging jet.

(a)

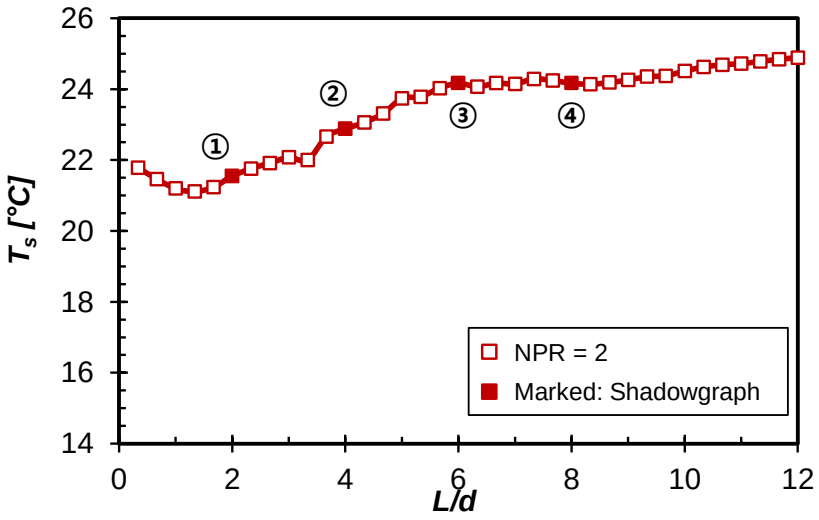

(b)

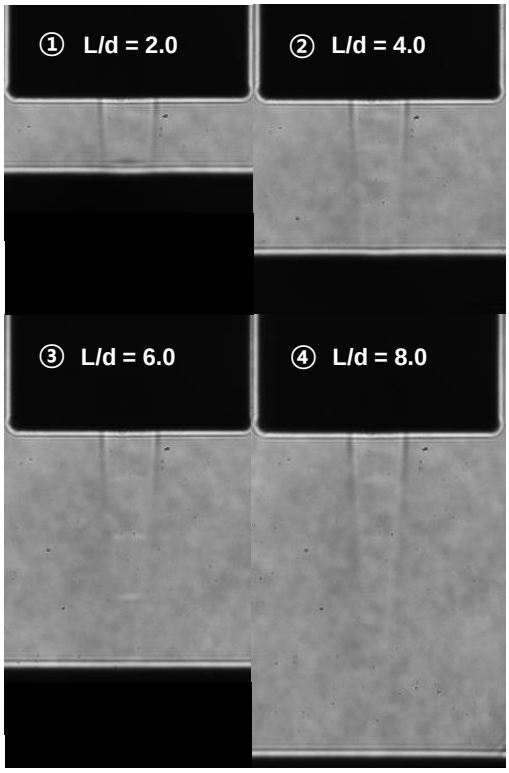

Figure 4.14. (a) Surface temperature and (b) flow shadowgraph with respect to *L/d* at *NPR = 2*

(a)

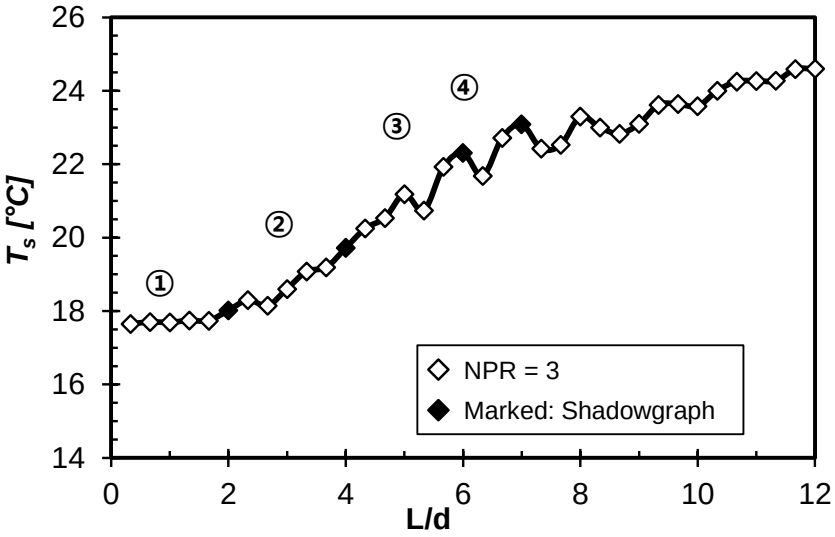

(b)

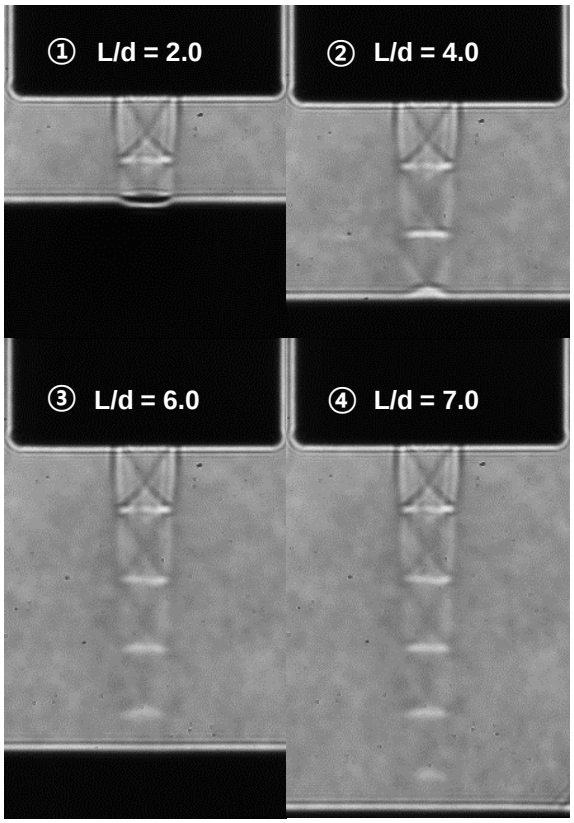

Figure 4.15. (a) Surface temperature and (b) flow shadowgraph with respect to *L/d* at *NPR = 3*

(a)

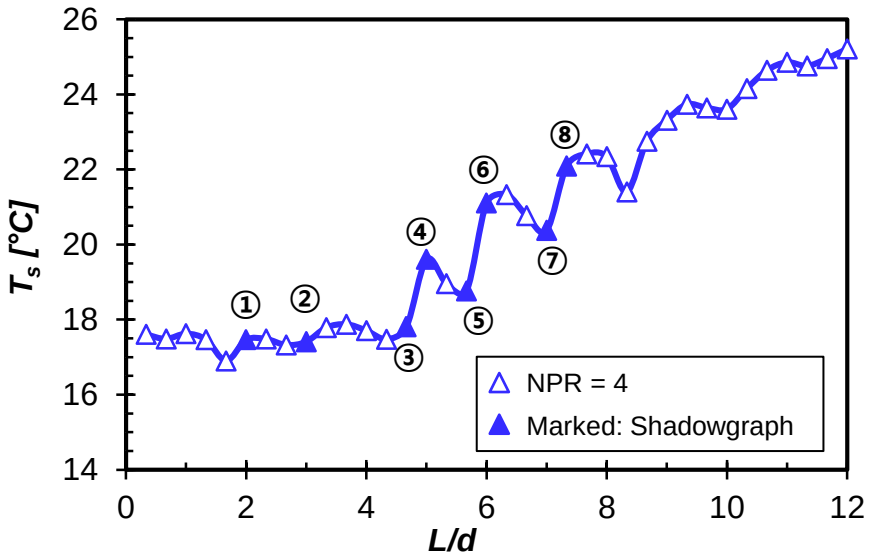

(b)

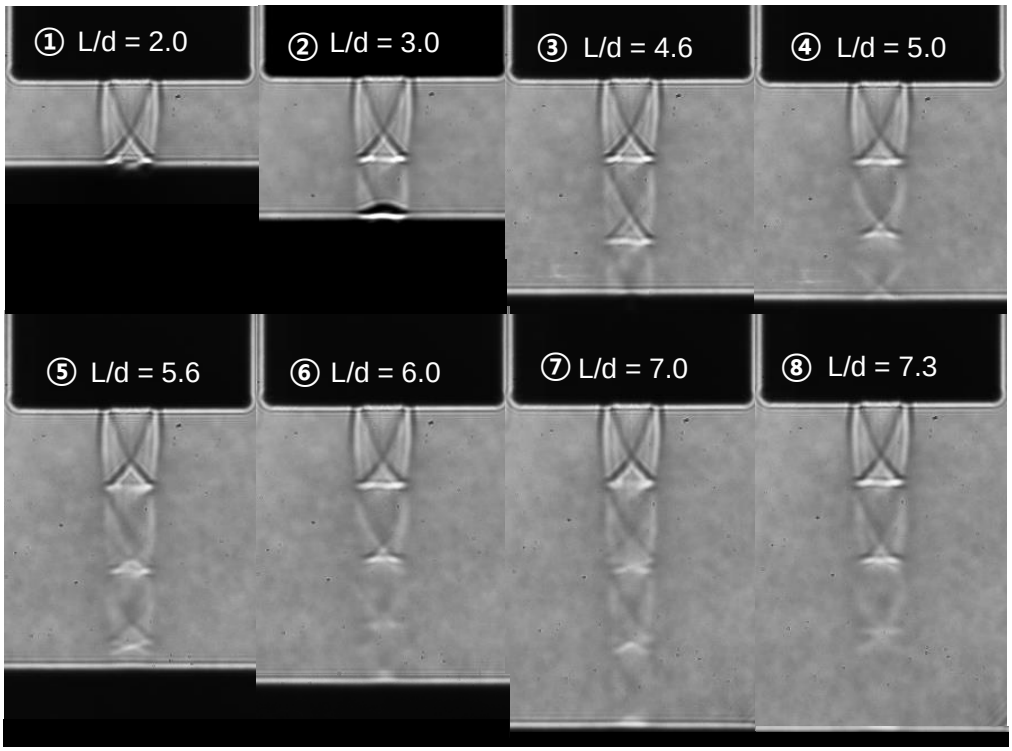

Figure 4.16. (a) Surface temperature and (b) flow shadowgraph with respect to *L/d* at *NPR = 4*

(a)

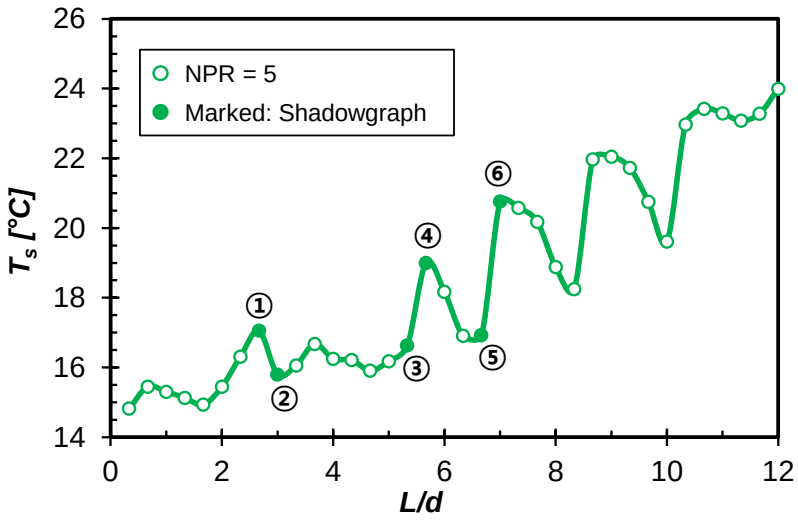

(b)

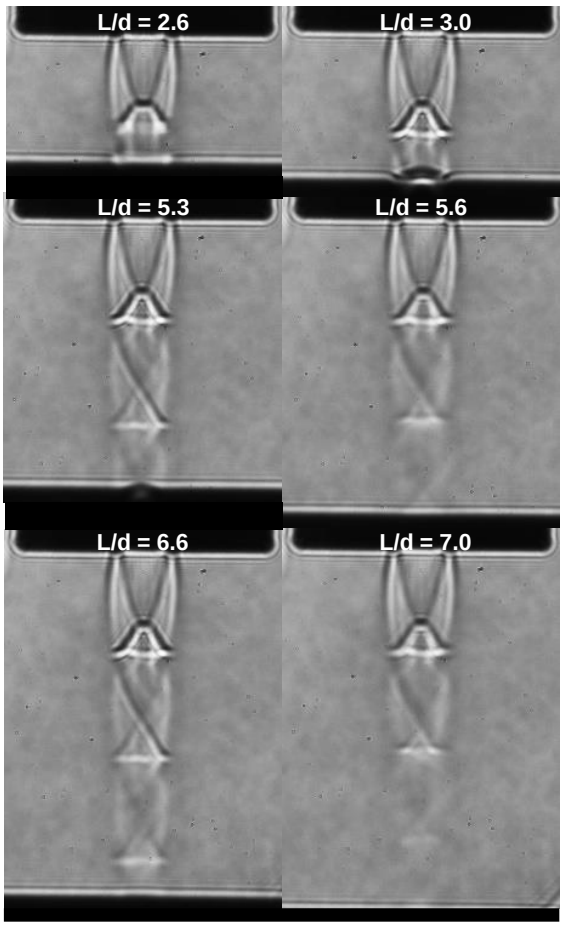

Figure 4.17. (a) Surface temperature and (b) flow shadowgraph with respect to *L/d* at *NPR = 5*

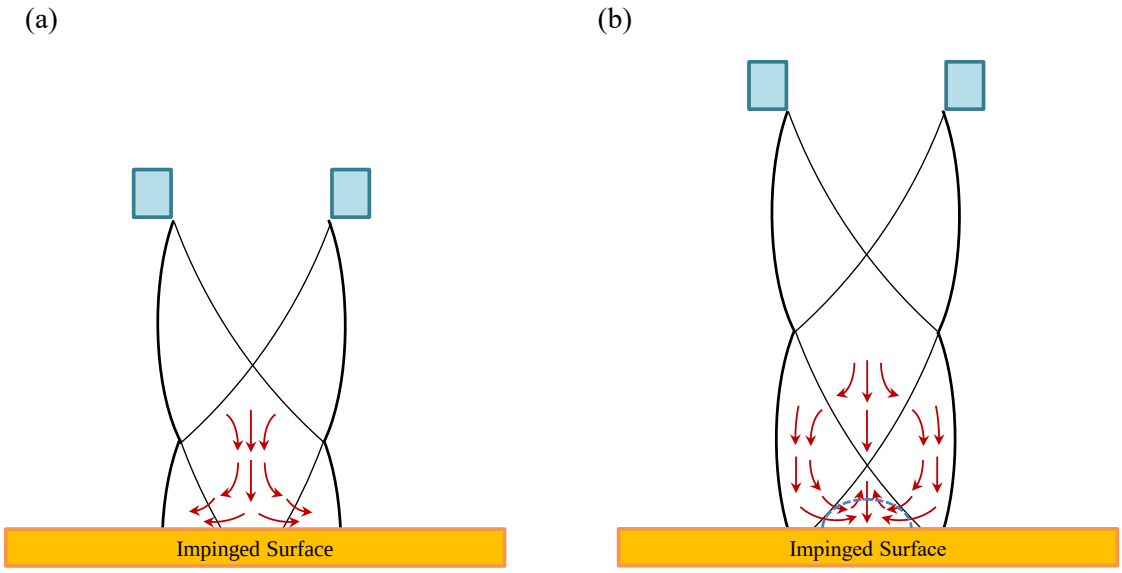

Figure 4.18. Recirculating flow direction according to location of target surface

Table 4.2. Parametric Study: Nozzle diameter and length

Case	1	2	3	4
Nozzle Diameter [mm]	1.5	1.5	1.5	1.0
Nozzle Length [mm]	10	15	20	10

4.2.3. Parametric study

Further investigations about supersonic under-expanded jet were performed by applying nozzle orifices which has different geometry in some cases. Nozzles shown in the schematic (Figure 3.2(a)) has two changeable parameters, which are nozzle length and nozzle diameter. Nozzle with *1.5 mm* diameter and *15 mm* length was used for this experiment. Nozzle length of *10 mm* and *20 mm* with *1.5 mm* diameter and nozzle diameter of *1.0 mm* with *15 mm* length were added to the experimental cases and performed in the same manner so far. In order for observation of distinguishing effect of nozzle length and diameter independently, experimental cases were chosen.

Effect of nozzle length was investigated as the surface temperatures represented in Figure 4.19. Figure 4.19(a) shows surface temperatures of *10 mm* length nozzle and Figure 4.19(b) shows the temperature of *20 mm* length nozzle. The basic characteristics of both graphs remain; larger NPR resulted intense flapping in each experiment. Though, the peak-to-valley amplitude in terms of temperature sets off the difference between them. In the case of *10 mm* nozzle, the maximum amplitude is shown *1.61 ℃* which is less than the almost doubled amplitude of counterparts, *3.21 ℃*. The amplitude of *20 mm* nozzle with *NPR = 4* has a maxima of 1.79 *℃*, which is even higher than *10 mm* nozzle with *NPR = 5*. This result indicates nozzle length definitely affects the degree of under-expansion and compressibility. Converged length constraint the jet fluid inside the tube and suppress the flows; resulting pressurizing jet fluid so that the nozzle exit pressure has grown eventually. In this meaning, NPR (nozzle-pressure ratio) couldn't represent practical pressure ratio because of the used pressure value of nozzle inlet and ambient. The pressure ratio between nozzle exit and ambient is expected to ascend if the flow is constrained tightly.

Besides, the effect of nozzle diameter was investigated as well. Schlieren images and surface temperatures are shown in Figure 4.20. The nozzle exit geometry was scaled, therefore, the captured shadowgraphs represents the differences in size of jet structures. When NPR is fixed, the jet downstream flow structures are proven to be similar, no matter what value the nozzle diameter is. Figure 4.20(a) shows the common trend of two different nozzles. The trend of shock structure could be supported by their surface temperature measurements, which is shown in Figure 4.20(b). Although the shock cell length is different, but the nozzle-to-plate spacing is non-dimensionalized by nozzle diameter so that the scaled shock cell length is reflected to the graph. Cyclic period of both nozzles are same since identical NPR is set in each experiment and constructed flow structures has same geometries. Starting from *L/d = 5.3*, both jets fluctuated four cycles. On the other hand, the amplitude fluctuations of *1.0 mm* nozzle is insufficient compared with *1.5 mm* nozzle. This represents the effect

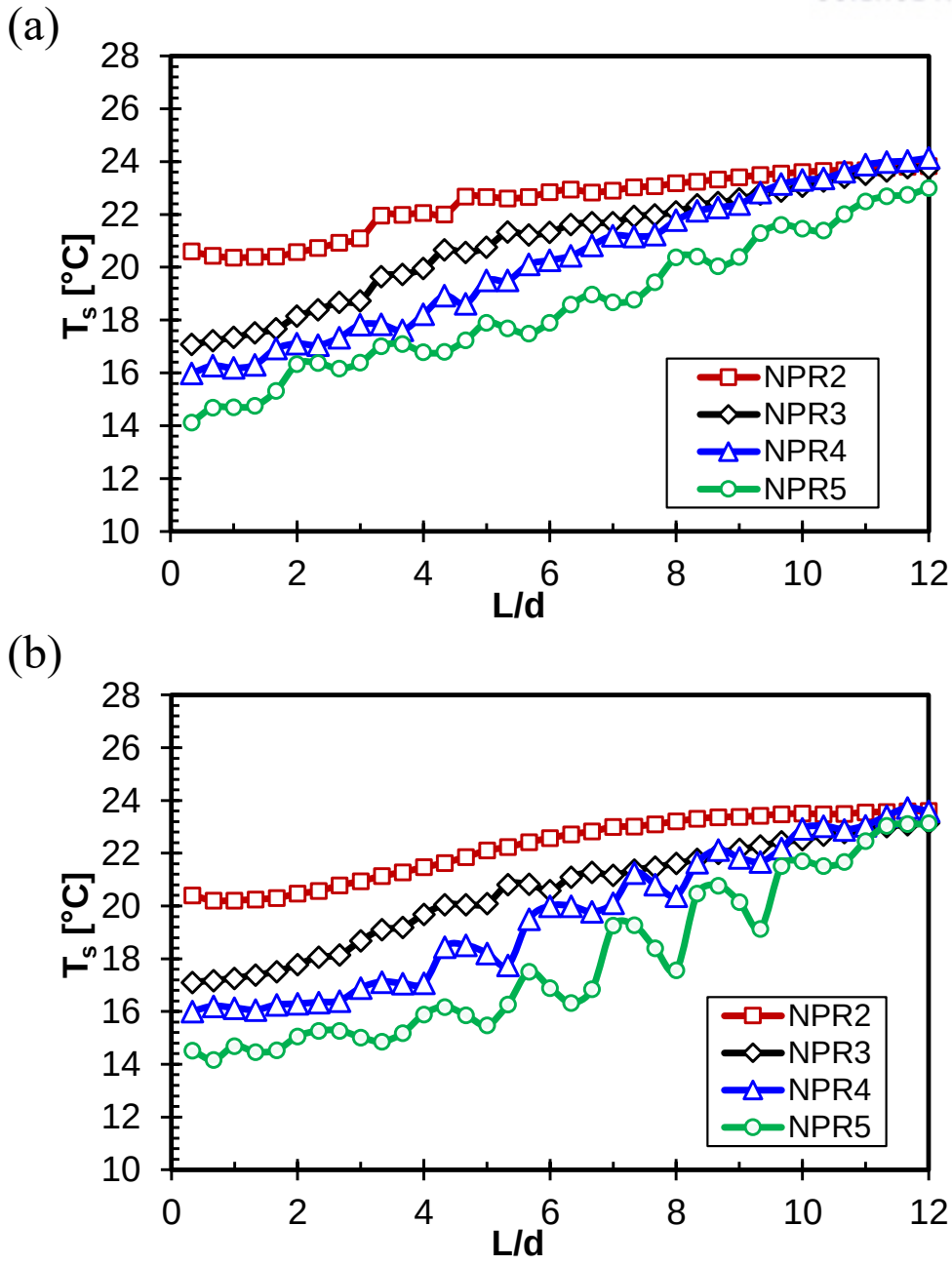

Figure 4.19. Surface temperature measurements with nozzle length of (a) 10 mm (b) 20 mm

(a)

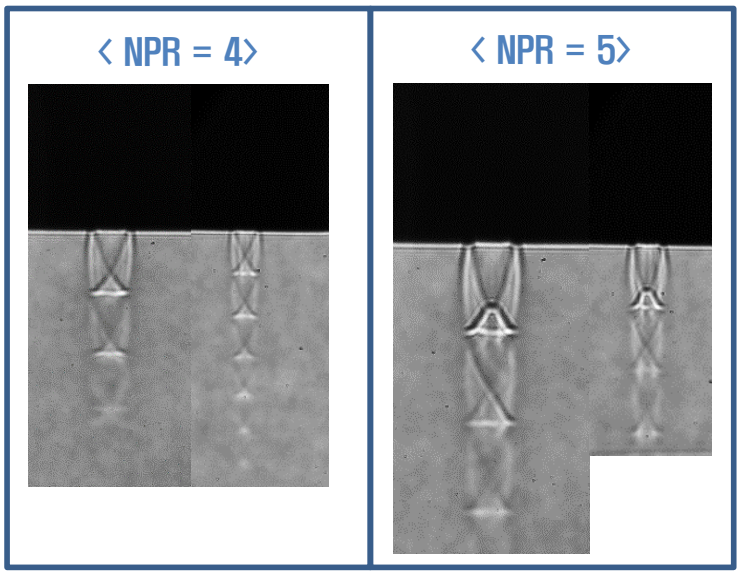

(b)

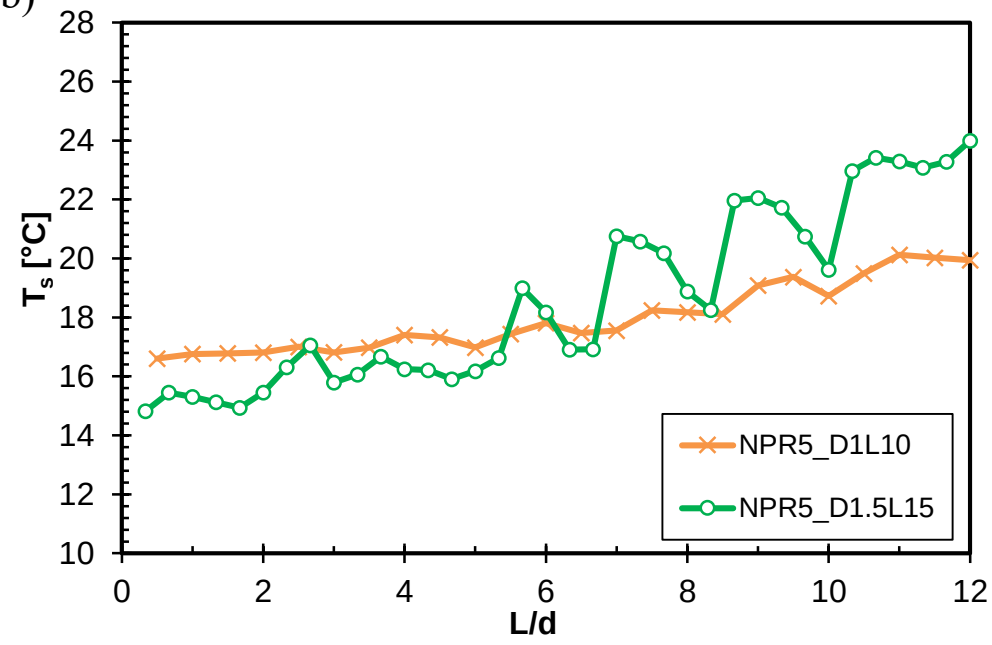

Figure 4.20. Comparison of (a) Schlieren images and (b) surface temperature between nozzle diameter of 1.0 mm and 1.5 mm

of nozzle diameter, which means that Reynolds number, jet flow velocity, Mach number and in particular, momentum carried by jet fluid are all reduced when decreased nozzle diameter is used. The less momentum is dissipated much faster than larger nozzle's case, therefore its compressible effects get weaken as well.

Nozzle geometry affects the nozzle exit condition, thus, nozzle exit temperature and pressure was determined by nozzle geometry. In this research, nozzle length and nozzle diameter were regarded as parameters. Especially, trend of temperature fluctuations depends on a ratio of nozzle diameter and length. The effect of nozzle configuration should be investigated as a future work, for further comprehension of temperature fluctuation phenomena with flow structures.

5. Conclusions

This research was performed to enhance the amount of heat transfer when gas-based impinging jet is used. Two main considerations to overcome gas jet's limitation were suggested in this study. In first part, sublimation process of CO_2 was included in cooling process. Since dry-ice particles are converting to CO_2 gas in atmospheric condition after all, no additional device/equipment are needed comparing with typical gas jet. On the other hand, the amount of heat transfer was increased because dry-ice particles absorbed additional heat from target surface by latent heat. In second part, the jet fluid velocity was accelerated into supersonic region. Jet fluid which has high flow rate/velocity/Reynolds number provides improved cooling performance. However, there is key characteristics of supersonic under-expanded impinging jet to the surface temperature. The temperature fluctuations according to nozzle-plate distance was investigated in the point of relationship between flow structures and heat transfer. The whole research was carried experimentally using open-loop impinging gas-jet system.

As an efficient heat transferring method, experiments of jet impingement were performed in this study. Especially, with nozzle diameter of *1.0 mm* and *1.5 mm*, effects of phase change and supersonic under-expansion were investigated respectively, in order to suggest a concept of two-phase jet including sublimation and to enhance the comprehension of supersonic under-expanded jet's heat transfer characteristics, preparing nearly approaching micro-scaled cooling applications.

Impinging jet heat transfer via a CO_2 jet was experimentally compared with that of a N_2 jet in terms of the stagnation temperature and the average surface convective heat transfer coefficient with various values of the Reynolds number and nozzle-to-plate spacing. The evaluated heat transfer coefficients for both gases jet generally show the established single phase jet trend with respect to the Reynolds number and nozzle-to-plate spacing variation. The surface cooling is improved when using a CO_2 jet. However, the heat transfer coefficient measurement indicates that the numbers from CO_2 jet are inferior to those of the N_2 Jet, because the reference temperature difference. Although the heat transfer coefficient of CO_2 is under-evaluated, it has a non-common diverging trend as the Reynolds number increases and the nozzle-to-plate spacing decreases, unlike the case of N_2, i.e., the CO_2 impinging jet has the potential to overcome the under-estimation by forming more dry-ice particles. The temperature acquired from the IR imaging shows the overall trends of the colder surface temperature for CO_2 jet impinged surface, which represents the better cooling performance. The test results reveal that the CO_2 dry-ice jet is shown to be better suited for cooling applications, especially for low-temperature operations.

Following experiments of supersonic under-expanded circular impinging jet was performed in

both points of heat transfer and flow field structures in terms of stagnation temperature of the surface and compared with images obtained by schlieren imaging. The various values of experimental parameters such as nozzle pressure ratio that covers moderate and highly under-expanded regions, resulted the differences in flow directions in each case. The heat transfer characteristics of supersonic jet is observed in terms of surface stagnation temperature measurements and the data are matched with flow field images in each experimental case. Temperature fluctuations in thermocouple measurements are related to the recirculation flow direction and location of the copper block's surface. When the recirculation is enhanced, the heat transfer performance becomes worth instead. This phenomenon is maximized if the stagnation point is on a reflected shock, making the flow field near the stagnation point become faint and lowering shock cell length. In addition, higher nozzle pressure ratio resulted more fluctuations in temperature data and clearer flow patterns since the compressible effect gets arisen if flow velocity is higher. Therefore, the performances of thermal energy transportation of supersonic impinging jets in stagnation region are highly related to the flow field patterns of the jet, in particular, recirculation flows and shock locations. In addition, parametric study using selected nozzles are carried and discussed. Both nozzle length and diameter affects the weak-to-valley amplitude of temperature fluctuations with respect to nozzle-to-plate distance (L/d). Constraint to the jet fluid through the nozzle converging geometry causes suppressed fluid flow at nozzle exit, resulting the compressibility effect arose. Also, reduced fluid momentum due to the decreased nozzle diameter represents less fluctuation in terms of surface temperature. In case study, nozzle length or diameter doesn't affect the shock cell length or shock cell period at jet downstream if the distance from the target surface is non-dimensionalized by nozzle diameter.

These heat transfer and flow field characteristics has the rest of further investigations when the jet flow velocity is in supersonic region, which is applicable in aerodynamic field and micro-flud dynamics as well.

REFERENCES

[1] R. Viskanta, “Heat Transfer to Impinging Isothermal Gas and Flame Jets”, Exp. Thermal and Fluid Science, Vol. 6, Issue 2, pp. 111-134, 1993.

[2] K. Jambunathan, E. Lai, M. A. Moss and B.L. Button, “A review of heat transfer data for single circular jet impingement”, Int. J. Heat Fluid Flow, Vol. 13, Issue 2, pp. 106-115, 1992.

[3] N. Zuckerman, N. Lior, “Jet Impingement Heat Transfer: Physics, Correlations, and Numerical Modeling”, Adv. Heat Transfer, Vol. 39, Issue 6, pp. 565-631, 2006.

[4] John H. Lienhard V., “Heat Transfer by Impingement of Circular Free-Surface Liquid Jets”, ISHMT-ASME Heat and Mass Transfer Conference, 2006.

[5] Christopher K.W. Tam, “Influence of Nozzle Geometry on the Noise of High-speed Jets”, J. AIAA, Volume 36, Issue 8, pp. 1396-1400, 1998.

[6] M. T. Meyer, I. Mudawar, C. E. Boyack and C. A. Hale, “Single-phase and two-phase cooling with an array of rectangular jets”, Int. J. Heat Mass Transfer, Vol. 49, Issue 1-2, pp. 17-29, 2005.

[7] D. Singh et al., “Effect of Nozzle Shape on Jet Impingement Heat Transfer from a Circular Cylinder”, Int. J. Thermal Sciences, Volume 96, pp. 45-69, 2015.

[8] J. San, C. Huang and M. Shu, “Impingement cooling of a confined circular air jet”, Int. J. Heat Mass Transfer, Vol. 40, Issue 6, pp. 1355-1364, 1997.

[9] A. Abdel-Fattah, F. Sh. Abou-Taleb and Gamal H. Moustafa, “Behavior of Air Jet Impinging on Curved Surfaces”, J. Aerospace Eng., Vol. 27, Issue 5, 2014.

[10] M. Rahimi, I. Owen and J. Mistry, “Impingement Heat Transfer in an Under-expanded Axisymmetric Air Jet”, Int. J. Heat and Mass Transfer, Vol. 46, Issue 2, pp. 263-272, 2001.

[11] C.F. Ma, Y.P. Gan, Y.C. Tian and D.H. Lei, “Liquid Jet Impingement Heat Transfer with or without Boiling”, J. Thermal Sci, Vol. 2, Issue 1, pp. 32-49, 1993.

[12] C.F. Ma, A.E. Bergles, “Jet Impingement Nucleate Boiling”, J. Heat Mass Transfer, Vol. 29, Issue 8, pp. 1095-1101, 1986.

[13] N. Seiler, J. Marie and O. Simonin, “Transition Boiling at Jet Impingement”, Int. J. Heat Mass

Transfer, Vol. 47, Issue 23, pp. 5059-5070, 2004.

[14] Zhen-Hua Liu, Jing Wang, “Study on film boiling heat transfer for water jet impinging on high temperature flat plate”, Int. J. Heat Mass Transfer, Vol. 44, Issue 13, pp. 2475-2481, 2000.

[15] Richard R. Parker et al., “Supersonic Two-Phase Impinging Jet Heat Transfer”, J. Heat Transfer, Volume 135, 2013.

[16] R. Sherman, “Carbon Dioxide Snow Cleaning”, Int. J. Particulate Science and Technology, Vol. 25, Issue 1, pp. 37-57, 2007.

[17] R. Sherman, P. Adams, “Carbon Dioxide Snow Cleaning”, Particles on Surfaces 5, VSP, pp. 221-237, 1999.

[18] K.W. Everitt and A.G. Robins, "The Development and Structure of Turbulent Plane Jets”, J. Fluid Mechanics, Volume 88, Issue 3, pp. 563-583, 1978.

[19] T.C. Adamson Jr., “On the Structure of Jets from Highly Underexpanded Nozzles Into Still Air”, J. Aerospace Sciences, Vol. 26, Issue 1, pp. 16-24, 1959.

[20] P. Deogonda, V. N. Chalwa, M. C. Murugesh, V. Dixit. “Wall Static Pressure Distribution Due to Confined Impinging Circular Air Jet”, Int. J. Research in Engineering and Technology, Vol. 3, Issue 3, pp. 591-597, 2014.

[21] F.S. Alvi, J.A. Ladd and W.W. Bower, “Experimental and Computational Investigation of Supersonic Impinging Jets”, J. AIAA, Vol. 40, Issue 4, pp. 599-609, 2012.

[22] A. Krothapalli et al., “Flow Field and Noise Characteristics of a Supersonic Impinging Jet”, J. Fluid Mechanics, Volume 392, pp. 155-181, 1999.

[23] M. Dharavath and D. Chakraborty, “Numerical Simulation of Supersonic Jet Impingement on Inclined Plate”, J. Defence Science, Vol. 63, Issue. 4, pp. 355-362, 2013.

[24] J. Song et al, “Thermal Characteristics of Inclined Plate Impinged by Underexpanded Sonic Jet”, Int. J. Heat and Mass Transfer, Volume 62, pp. 223-229, 2013.

[25] Y. Nakai, N. Fujimatsu and K. Fujii, “Flow Classification of the Under-Expanded Super Sonic Jet Impinging on a Flat Plate”, 33rd AIAA Fluid Dynamics Conference and Exhibit, 2003.

[26] M. Angioletti et al., “Simultaneous Visualization of Flow Field and Evaluation of Local Heat

Transfer by Transitional Impinging Jets", Int. J. Heat and Mass Transfer, Volume 46, Issue 10, pp. 1703-1713, 2003.

[27] Lemmon, E.W., Huber, M.L., McLinden, M.O. NIST Standard Reference Database 23: Reference Fluid Thermodynamic and Transport Properties-REFPROP, Version 9.1, National Institute of Standards and Technology, Standard Reference Data Program, Gaithersburg, 2013.

[28] J. R. Roebuck, T. A. Murrell, E. E. Miller, "The Joule-Thomson effect in carbon dioxide", J. Am. Chem. Soc., Vol. 64, Issue 2, pp. 400-411, 1941.

[29] E.S. Burnett, "Experimental study of the Joule-Thomson effect in carbon dioxide", Phys. Rev., Vol. 22, Issue 6, pp. 590-616, 1923.

[30] J. Lee, S. Lee, "Stagnation region heat transfer of a turbulent axisymmetric jet impingement", Exp. Heat Transfer, Vol. 12, Issue 2, pp. 137-156, 1999.

[31] K. A. Phalnikar, R. Kumar, F. S. Alvi, "Experiments on free and impinging supersonic microjets", J. Exp. Fluids, Vol. 44, pp. 819-830, 2008.

ACKNOWLEDGEMENTS

Lots of support, encourages and concerns for me and my research helped me to complete present study. With great honor, I would like to express appreciation to people who supported and assisted my works during Master's courses in UNIST.

At first, I would like to appreciate sincerely my adviser Assisitant Professor, Dr. Jaeseon Lee. I've studied gladly and had much experiences in engineering under his considerate and continuous guidance. By Dr. Jaeseon Lee's favor, this research could be well forward and progressed by this time. I would respect his admirable knowledge and passion to the research. I looked up to him as my mentor, and also, I will.

I would like to appreciate encourages of Professor Dr. Hyungson Ki and Professor Dr. Jaesung Jang as well, who gave sincere advices for this research. I'm really grateful to get their heartiest concerns in whole time.

I cannot help mentioning my dear laboratory members and friends. They supported me by both materially and spiritually during the research. It would be impossible to finish my work without them.

Also, my family members who kept encouraging me and became a good counselor when I struggled to deal with several obstacles. Their gentle advices provided me a driving force to keep studying.

Lastly, for people whom I did not mention the name, I would not forget the gratitude toward them and thank to them too.

Dongsu Kim